

Supplementary Materials for  
**Feasibility of keeping Mars warm with nanoparticles**

Samaneh Ansari *et al.*

Corresponding author: Edwin S. Kite, kite@uchicago.edu

*Sci. Adv.* **10**, eadn4650 (2024)  
DOI: 10.1126/sciadv.adn4650

**This PDF file includes:**

Supplementary Text  
Figs. S1 to S19  
Tables S1 to S3  
References

## Supplementary Text.

### 1. Calculation of optical properties of nanorods.

Simple calculations (e.g., ref. 17) suggest that 9  $\mu\text{m}$  long conductive nanorods with a 60:1 aspect ratio would have a strong and broad extinction in the  $\sim 22 \mu\text{m}$  spectral window. To test this, we carried out finite-difference time domain simulations (FDTD: 3D Electromagnetic Simulator). First, we verified that the FDTD simulations reproduce Mie theory for water ice spheres (49) (Fig. S1). The nanorod FDTD simulations use a pulse of light whose interaction with the simulated nanoparticle is Fourier-decomposed to obtain the  $\lambda$ -dependence of the absorption and scattering cross sections as well as the scattering asymmetry. The representation of the angular distribution of scattered light by a single parameter, the scattering asymmetry, is standard in climate modeling (e.g., 28). 75 wavelengths, approximately log-uniformly spaced from 0.24-55  $\mu\text{m}$ , are obtained (Table S1). We used refractive indices for Fe from Ref. 50, and for Al from Ref. 51. Ref. 52 suggest that Fe refractive indices obtained prior to their own work might be affected by Fe-oxidation, but as Mars' atmosphere is  $\sim 0.1\%$   $\text{O}_2$  some degree of oxidation is inevitable, so this is acceptable. Implementation involved combining three different simulations for different  $\lambda$  ranges, for computational feasibility. 75 simulations were carried out for the 9  $\mu\text{m}$  long nanorod, corresponding to the product of 5 orientations in  $\theta$ , 5 orientations in  $\varphi$  ( $0^\circ$ ,  $30^\circ$ ,  $45^\circ$ ,  $60^\circ$ , and  $90^\circ$ , for both angles), and three  $\lambda$  ranges. Here,  $\theta$  corresponds to rotations in the E-H plane and the other rotation is termed  $\varphi$  (k-E plane, symmetric and similar to k-H plane) (Fig. S2). Far-field methods were employed to obtain the scattering phase function. We anticipate that actual nanorods will have circular cross-sections. Because of computational limitations associated with the FDTD approach, we model a nanorod with square cross-section, but find that switching between circular and square cross-sections makes negligible difference to the calculated optical properties (Fig. S3).

As expected, the simulated nanorods showed strong, broad absorptions near 22  $\mu\text{m}$  (Fig. 1), supporting their suitability for Mars warming. This is consistent with previous work on Ag nanorods (53). The wavelength of the absorption peak is slightly longer than double the rod length, due to plasma effects (54). In order to average over orientations (Fig. S4), rod orientation was uniformly sampled on the sphere relative to the incident electric field vector ( $\sim 1000$  samples between  $0^\circ$  and  $90^\circ$  for both angles) and optical properties interpolated using a spline in the grid of 25 computed orientations for each  $\lambda$ . The orientations of nanorods in the atmosphere are assumed to be random and uniform, hence averaging over a spherically equidistant grid of orientations would result in proper orientation-averaged characteristics. We found (minor) infrared back-scattering in these simulations. A sensitivity test using the 3D model for Fe nanorods showed that this choice makes little difference ( $\sim 0.3 \text{ K}$ ) to the calculated temperatures.

To check the interpolation accuracy, we did check runs on multiple intermediate points (Fig. S5). When the rod is viewed nearly end-on, the interpolation results grow less accurate. However, end-on geometries are infrequently encountered, and at the higher angles, the scattering and absorption cross-sections are substantially smaller, so the effect of these points on the overall orientation average is insignificant. To check the simulation accuracy, we did a check run increasing the

resolution across the width of the nanorod from 8 simulation mesh points (20 nm spacing) to 10 simulation mesh points (16 nm spacing), finding negligible differences (Fig. S6).

We also did calculations for 7.5  $\mu\text{m}$ -long Fe nanorods with cross-section  $0.08 \mu\text{m} \times 0.08 \mu\text{m}$ , finding peak extinction around 20  $\mu\text{m}$  (Fig. S7), and less climate warming per nanorod, but more climate warming per kg of nanorods. An optimal warming approach might use a mix of rods of different lengths. Moreover, we find that the total extinction (absorption plus scattering) for Al nanorods is the same as for Fe nanorods (Fig. S8), and the corresponding warming is also about the same (Table S2), even though the density of Al is three times less than that of Fe. Fe, Al, and Mg are all present at  $>4 \text{ wt}\%$  level in Mars soil. We focus here on Al and Fe because optical properties are available over the full wavelength range of interest (other metals are worthy of future investigation). This suggests that further research might yield further improvements in the effectiveness of warming.

## 2. Calculation of the surface-warming effect of the nanorods using 1D climate model.

Our single-column radiative-convective climate model (RCM) subdivides atmospheres into multiple vertical log-layers (we implement 201 layers here) that extend from the ground to the top of the atmosphere ( $1 \times 10^{-5}$  bar here) (e.g. 25). The RCM has 55 infrared and 38 solar spectral intervals (55). The model applies a standard moist convective adjustment (e.g. 56). Should tropospheric radiative lapse rates exceed their moist adiabatic values, the model relaxes to a moist  $\text{H}_2\text{O}$  adiabat at high temperatures or to a moist  $\text{CO}_2$  adiabat when temperatures are low enough for  $\text{CO}_2$  to condense. The RCM implements a standard solar spectrum (57). For present Mars (solar flux =  $585 \text{ W/m}^2$ ), we assume a typical stratospheric temperature of 155 K and a surface albedo of 0.22 (e.g. 24). The atmospheric pressure is a Mars-like 650 Pa with an assumed acceleration due to gravity of  $3.73 \text{ m/s}^2$ . Although we prescribe a tropospheric relative humidity of 50%, our results are insensitive to this parameter. The baseline mean surface temperature of the resultant pure  $\text{CO}_2$  atmosphere (without nanorods) is 218 K. For comparison, Mars' observed global mean surface temperature is 202 K (10). The 1D model runs warmer in the 6 mbar no-nanorods case mainly because it lacks day-night and equator-pole temperature contrast, and because it lacks clouds, dust and topography (10). With an assumed surface albedo of 0.22 and solar flux of  $585 \text{ W/m}^2$ , the predicted equilibrium temperature ( $T_{eq}$ ) would be  $\sim 212 \text{ K}$  (assuming a perfect blackbody). This 212 K  $T_{eq}$  value is the minimum surface temperature for a 1D model with no greenhouse effect. However, our 1D model predicts 6 K greenhouse effect (consistent with data and with other models), raising the mean surface temperature to  $\sim 218 \text{ K}$  (e.g. 58). In summary, the warm 1D model output gives a useful benchmark comparison on the importance of 3D factors like dust, clouds and topography on modeling predictions in comparison with that from the nanorods.

One of the reasons for the differences in temperature response between the models is the baseline surface temperature, which is higher in the 1D model (for reasons explained above). The main cause, however, is differences in the vertical temperature profiles across models (e.g., Fig. S18). For instance, lapse rates differ slightly (the top of the cloud deck is at a slightly higher pressure level, or closer to the ground, in the 3D model) and the 3D model has a near-surface temperature inversion which is absent in the 1D code (Fig. S18). The 3D model also has a larger effective

convective region. Tests confirm that the 1D and 3D results agree more closely when the 3D profile is imposed on the 1D model. For example, at  $\tau_{\text{Fe}} = 0.25$ , imposing the same mean surface temperature in the 1D model as is obtained for the 3D model ( $\sim 225.5$  K) yields a top-of-atmosphere (TOA) net outgoing longwave radiation/net incident stellar flux ratio of  $\sim 0.69$  (a value equal to 1 corresponds to a TOA radiative equilibrium). In other words, the 1D model “wants” to warm. However, when the 3D model vertical temperature profile was applied instead (at the same surface temperature), this ratio had increased to 0.86 (removing  $\sim 60\%$  of the difference from 1). In other words, most of the difference between the 3D model and the 1D model can be explained by differences in the vertical thermal profile. This suggests that even across 3D models, differences in convective schemes (and temperature profiles) could produce some spread in the results, motivating investigation of engineered warming of Mars using different 3D schemes. Despite these numerical differences, the atmospheric response to nanorod addition in both the 1D and 3D models is qualitatively very similar. In both cases, nanoparticle warming provides a greenhouse effect  $>5,000\times$  greater than the current state of the art.

Following Refs. 24-25, we calculate the wavenumber-dependent optical depths ( $\tau$ ) for the nanorods from the following expression:

$$\tau = 3 Q_{\text{eff}} NRC \Delta z / (4 r \rho) \quad (2)$$

Here,  $NRC$  is the nanorod content ( $\text{g}/\text{m}^3$ ) and  $\Delta z$  is the path length. This equation differs from (1) only in that the optical depth is integrated over all nanorod heights and across all wavenumbers, not just in the spectral window. The nanorods are well-mixed throughout the atmosphere (up to 35 km) above the imposed 500 Pa nanorod-layer base and so  $NRC$  was assumed to scale linearly with the local pressure. We computed the radius of the sphere with the equivalent nanorod volume, which yields an effective nanorod particle radius of  $\sim 0.38$   $\mu\text{m}$  for the 9  $\mu\text{m}$  nanorods.

Within the 1D model framework, we implement a simple procedure to calculate nanorod warming. For each assumed nanorod optical depth, we find the surface temperature that yields stratospheric energy balance (i.e. the net outgoing and net incoming fluxes must balance each other) (Figs. S16-S17).

### 3. Calculation of the surface-warming effect of the nanorods using 3D climate model.

The FDTD output is interpolated to 2000 log-uniformly spaced  $\lambda$ 's. We set optical properties at  $\lambda > 55$   $\mu\text{m}$  equal to those at 55  $\mu\text{m}$  (Fig. S9). This approximation is acceptable, because extinction ( $\text{W}/\text{m}^2/\mu\text{m}$ ) is minor at such long  $\lambda$ . MarsWRF uses a two-stream radiation code (e.g. 22, 59). Radiative transfer calculations include both gas (for this work,  $\text{CO}_2$ ) and aerosol (for this work, natural dust, nanorods, and  $\text{CO}_2$  ice) radiative effects. This implementation of MarsWRF uses Planck-weighted averaging to bin down high-spectral-resolution optical properties. The blackbody temperature used for the Planck-weighted averaging is 6000 K for solar bands (6 bins from 0.24-4.5  $\mu\text{m}$ , with bin edges at 0.24, 0.40, 0.8, 1.31, 1.86, 2.48, 3.24, and 4.5  $\mu\text{m}$ ), and 215 K for the thermal infrared bands (6 bins from 4.5-1000  $\mu\text{m}$ , with bin edges at 4.5, 8.0, 12.0, 14.1, 16.0, 24.0,

60, and 1000  $\mu\text{m}$ ) (Fig. S9). Thermal equilibrium between gas and dust is assumed. We neglect radiation pressure, magnetic effects, quantum size effects, and temperature dependence of the optical constants.

In the fixed-cloud runs, present-day Mars values are used for orbital parameters, surface albedo, and surface thermal inertia. Mars' southern summer solstice occurs near perihelion, so (by Kepler's second law) northern summer is long and relatively cool, and southern summer is short and warm relative to annual average (Figs. S10-S12). Water vapor abundance in the atmosphere is fixed to zero, which is conservative in that water vapor radiative feedback would increase warming. A prescribed natural dust aerosol distribution is imposed corresponding to the Mars Climate Database MGS-dust-scenario (60), giving an average dust optical depth of 0.20 (peaking at 0.43 during southern summer). Natural dust aerosol warms the atmosphere but lowers daytime surface temperature. The artificial-aerosol layer is parameterized by a layer-base pressure (in Pa), a layer vertical thickness (in units of model levels), and the nanorod orientation-averaged optical depth at a reference  $\lambda$  (0.67  $\mu\text{m}$ ). Because the model levels are specified in  $\eta$  coordinates (where  $\eta = P/P_{\text{surf}}$ , where the model-top pressure has been subtracted from both pressures), the aerosol layer is physically more compact over the poles because low temperatures compact the air column. We refer to the altitude away from the poles below which 95% of the particles are contained as the "aerosol layer top height". The nanorod mixing ratio is assumed to be uniform within the nanorod layer (Fig. S13). We prescribe a layer-base level of 500 Pa and vary the layer thickness. This approach gives a maximum in artificial-aerosol opacity above the surface, which is also observed for natural Mars dust aerosol for some seasons (61-63). However, natural dust on Mars persists all the way to the surface (63) which has average pressure  $\sim 600$  Pa. This has no effect on our conclusions, as results are only weakly sensitive to the vertical distribution of simulated aerosol - for example, in Table S3, the "Thinner cloud (200 Pa base, 8 levels)" run differs from the reference case with 500 Pa base by only 0.3 K in average temperature. Buffering by latent heat implies that melting either ice cap to form seas would take at least centuries.

Settling for a 0.1  $\mu\text{m}$ -radius dust particle for 1 scale height at Mars surface pressure takes 3 years (Murphy 1990). Extrapolation to Al nanorods with radius 0.04-0.08  $\mu\text{m}$  suggests settling times that are similar or greater. Increase of Mars' atmospheric  $p\text{CO}_2$  under warming will decrease the Knudsen number and hinder dust settling. One-pass settling rates are much slower than that of natural Mars dust, and effective particle lifetime will be longer due to re-entrainment.

The runs presented here use a horizontal resolution of  $5.625^\circ \times 3.75^\circ$ , corresponding to a grid of 64 points in longitude  $\times$  48 points in latitude. A 40-layer vertical grid is used, using a modified- $\eta$  (terrain-following) coordinate ( $\eta = P/P_{\text{surf}}$ , where the model-top pressure has been subtracted from both pressures). The dynamical timestep varies between runs but is never longer than 1-min. The planetary boundary layer scheme is based on that in Ref. 64 (Medium-Range Forecast model scheme), with Mars implementation similar to that in Ref. 20, and the surface layer uses a Monin-Obukhov scheme. Runs are initialized from a cold state and continue until the simulated annual seasonal cycle is highly repeatable from year to year. We found that runs require only a single year of spin-up adjustment, as modern Mars, lacking seas, has low effective thermal inertia. Output is reported from the third year of each model run. Mean wind speed  $\sim 30$  m above the surface

increases from 8 m/s in the no-nanorods case to 13 m/s in the Fig. 2a (with-nanorods) case, which would stir up more dust (and nanorods). Daytime near-surface turbulence on Mars is sufficient to loft dust (and therefore nanorods) released at 10-100m altitude at all latitudes for  $P > 6$  mbar. Sensitivity tests adjusting model resolution, and varying nanorod distribution and other parameters are listed in Table S3.

For the no-nanorods case (Fig. 2b), the global and annual average shortwave radiation reaching the surface is  $133.1 \text{ W/m}^2$  ( $119.7 \text{ W/m}^2$  direct beam and the remainder diffuse/scattered), of which  $104.2 \text{ W/m}^2$  is absorbed with the rest being reflected. The spatially- and time-averaged surface albedo, including ice, is 0.237. The global/annual average longwave radiation at the surface (greenhouse effect) is  $23.9 \text{ W/m}^2$ . The global/annual average longwave emission from the surface is  $125.4 \text{ W/m}^2$ . The mismatch of  $-2.7 \text{ W/m}^2$  is caused by limited output sampling, fluxes into the surface (e.g.  $\text{CO}_2$  condensation, conduction), and model imprecision. For the with-nanorods case shown in Fig. 2a, the global and annual average shortwave radiation reaching the surface is  $89.2 \text{ W/m}^2$  ( $41.4 \text{ W/m}^2$  direct beam), of which  $70.6 \text{ W/m}^2$  is absorbed with the rest being reflected. The spatially- and time-averaged surface albedo, including ice, is 0.208. A greater fraction of sunlight is absorbed due to reduction in reflective seasonal  $\text{CO}_2$  ice. The global/annual average longwave radiation at the surface (greenhouse effect) is  $186.2 \text{ W/m}^2$ . The global/annual average longwave emission from the surface is  $254.3 \text{ W/m}^2$ . The mismatch of  $-2.5 \text{ W/m}^2$  (i.e., surface temperature under-stated relative to radiative fluxes) is caused by limited output sampling, fluxes into the surface (e.g.  $\text{CO}_2$  condensation, conduction), and model imprecision.

The runs shown in Fig. 2c correspond to optical depths at  $\lambda = 0.67 \text{ }\mu\text{m}$  of  $\{0, 0.125, 0.25, 0.5, 0.75, 1, 1.5, 2\}$ . Details for selected values are given in Fig. S14. The conversion factor is  $545 \text{ mg/m}^2$  for Fe and  $212 \text{ mg/m}^2$  for Al for one optical depth. Optical depths in the spectral windows are much greater than at  $0.67 \text{ }\mu\text{m}$  (Fig. 1). Output was sampled at 260 equally spaced intervals per Mars year. This provides (deliberately aliased) sampling of the day-night cycle during each season at each longitude and latitude. A sensitivity test using 1300 output steps showed negligible ( $\leq 0.1 \text{ K}$ ) differences in both annual-average and seasonal warming (Table S3). Mars' atmosphere is thin, with low thermal inertia and limited ability to transport heat laterally, and the tests with artificial imposed patchy or unsteady nanorod distribution show that the corresponding warming is sharply confined in space and time. This suggests that it might be possible to enhance warming at preferred latitudes and seasons. The atmosphere and surface temperature quickly responds to the radiative forcing at the release site/time, and after injection ceases, spreading of the particles away from the release site ensures that the warming at the release site soon decreases.

#### 4. Possible hazards.

Natural Mars air is unsafe for humans to breathe because it has almost no oxygen (insufficient for deflagration) and also has a high natural concentration of PM 2.5 (Mars mineral aerosol dust). The nanorod density is  $\sim 10 \text{ }\mu\text{g/m}^3$ , which would not substantially alter this situation. A more immediate concern is asbestosis, as humans would bring both natural dust and nanoparticles into settlements via airlocks. One way to mitigate this hazard would be to make nanorods that dissolve or fragment in liquid water.

## 5. Comparison to previous work.

To our knowledge, the most effective (on a per-unit-mass-in-the-atmosphere basis) Mars warming agent that has been previously been proposed is the "optimal [gas] mix" of ref. 8, which is mostly  $C_3F_8$  (molecular mass 188 Da). This gives 37.5 K warming for 1 Pa, which corresponds to  $170 \text{ kg/m}^2 \times (1 \text{ Pa} / 650 \text{ Pa}) \times (\sim 188 \text{ Da} / 44 \text{ Da}) \approx 1.1 \text{ kg/m}^2$ . This warming is about the same as the nanorod case shown in Fig. 2a, which corresponds to  $\sim 160 \text{ mg/m}^2$  of Al nanorods. Therefore this nanorod loading (using non-optimized nanoparticles) is  $>5000\times$  more effective than the optimal gas mix.

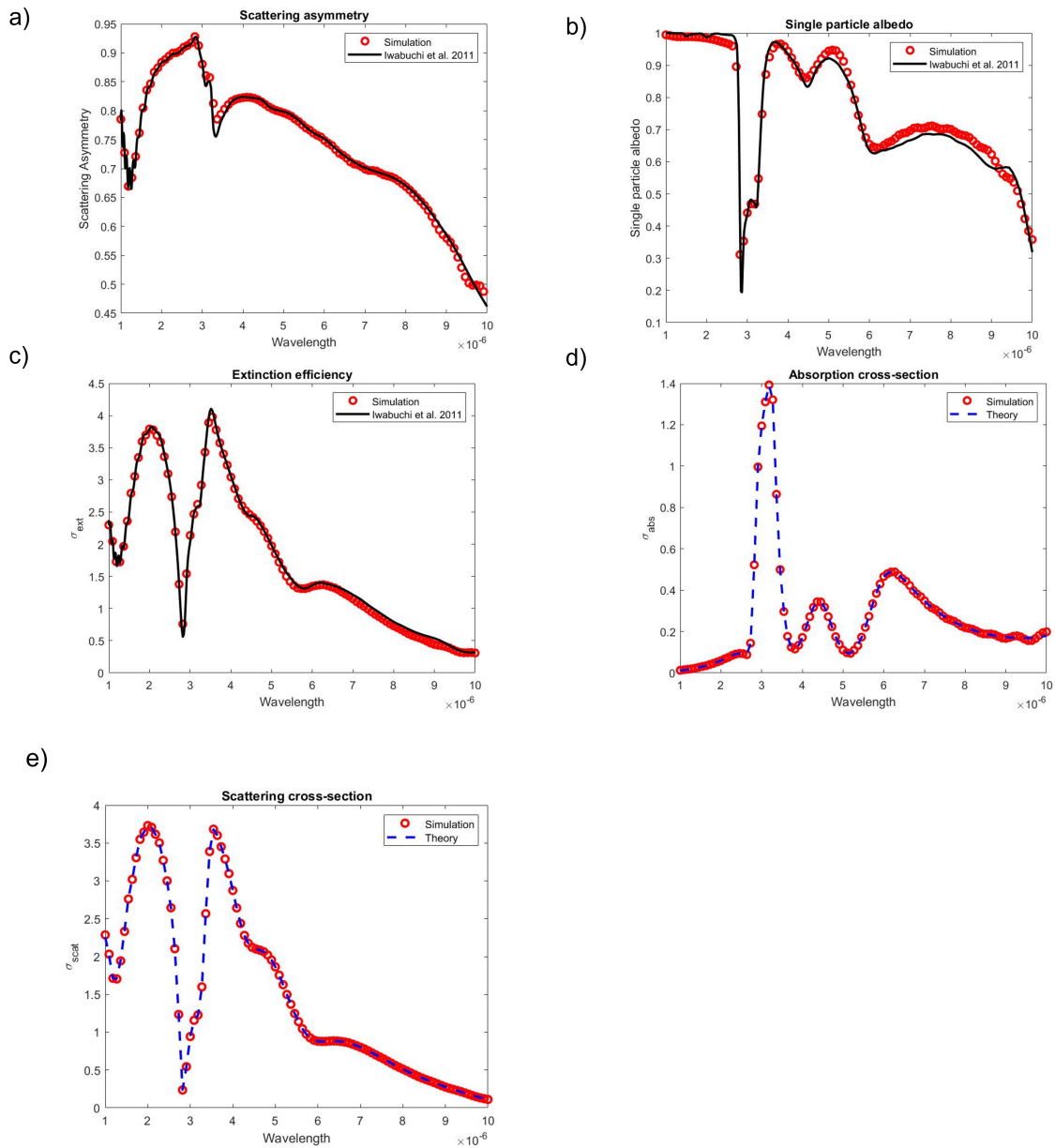


**Fig. S1.** (a,b,c) Verification of calculations by comparison to Mie-theory results for a water-ice sphere (49), showing single particle albedo, scattering asymmetry, and extinction efficiency. (d,e) Shows the comparison of analytical Mie scattering results for an ice sphere with simulation outputs.

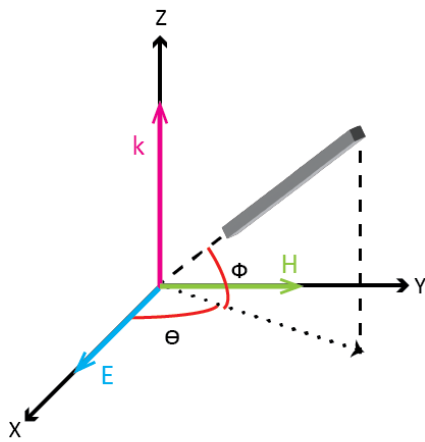


**Fig. S2.** Illustration showing the definition of the angles  $\theta$  and  $\varphi$  in the FDTD calculation. "k" corresponds to the direction of the propagation of the incident electromagnetic wave. The gray bar corresponds to the nanorod.

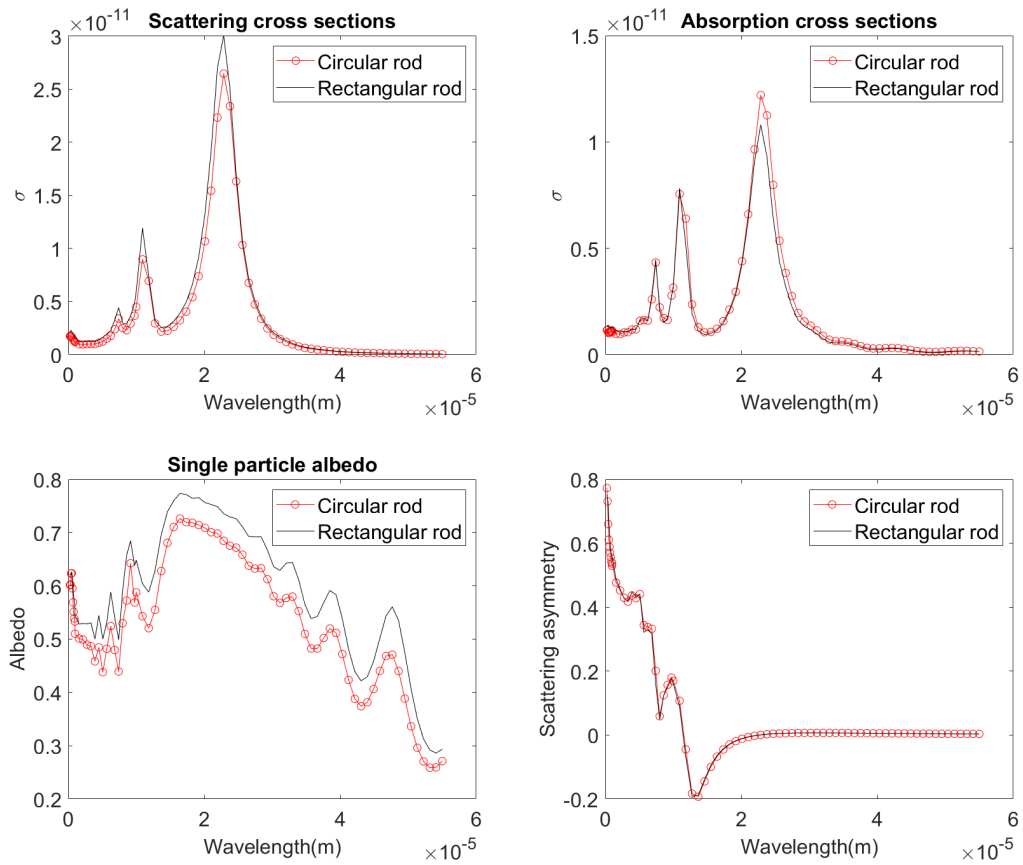


**Fig. S3.** Switching between a square and circular cross-section for the nanorod has only minor effects on the calculated optical properties. Fe nanorod, 9  $\mu\text{m}$ -long,  $\sim 60:1$  aspect ratio, orientation:  $\theta = 45^\circ$ ,  $\varphi = 45^\circ$ .

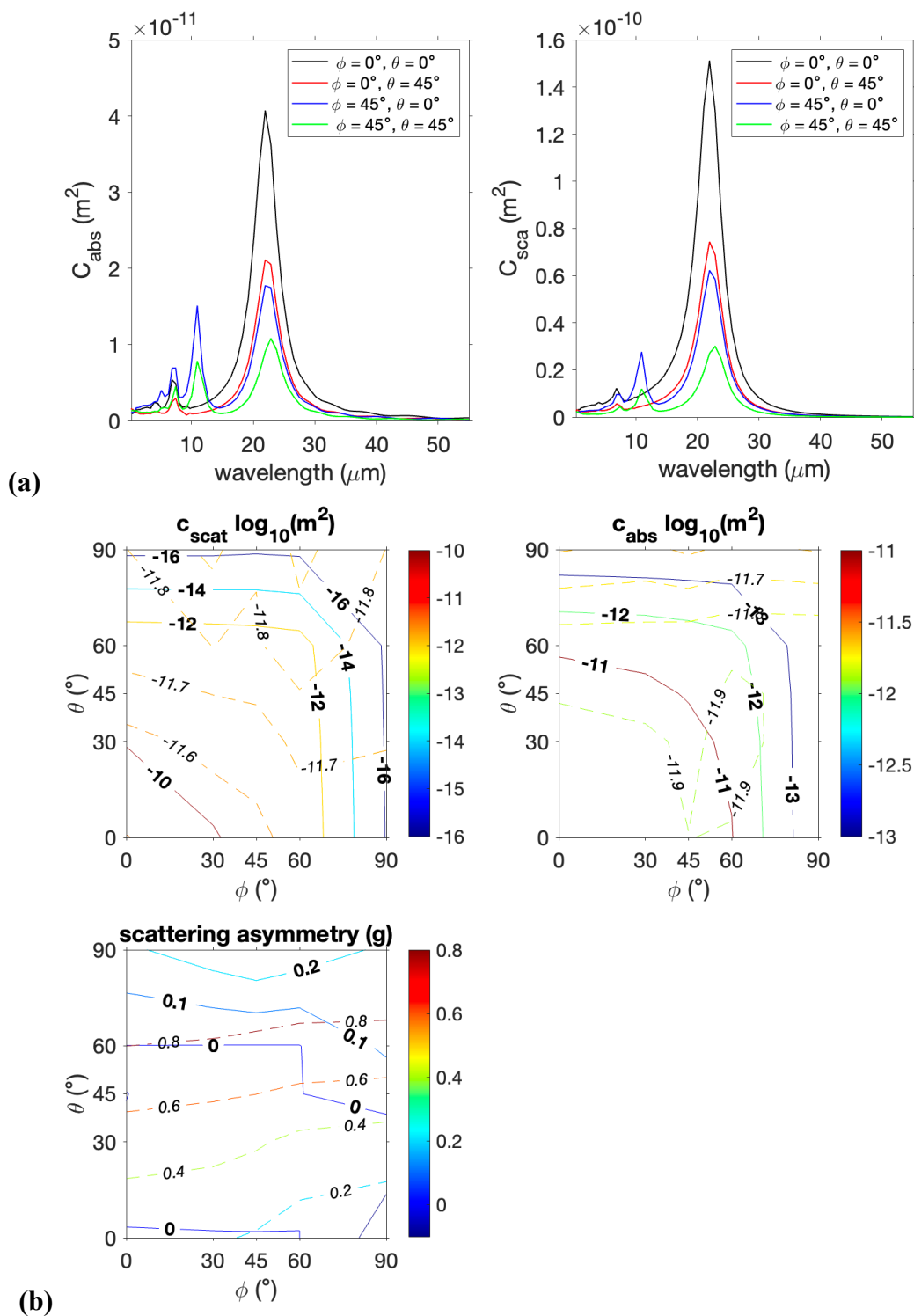
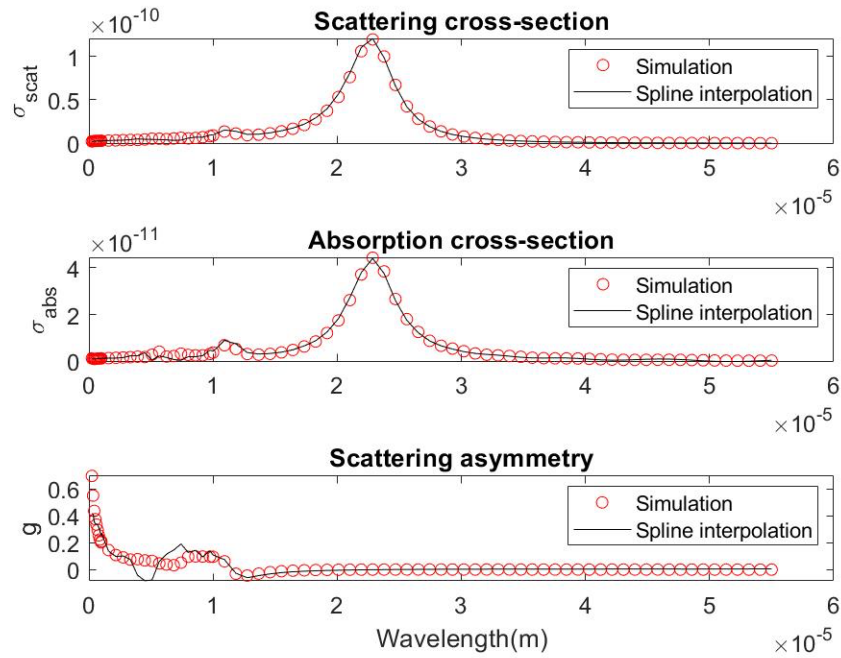
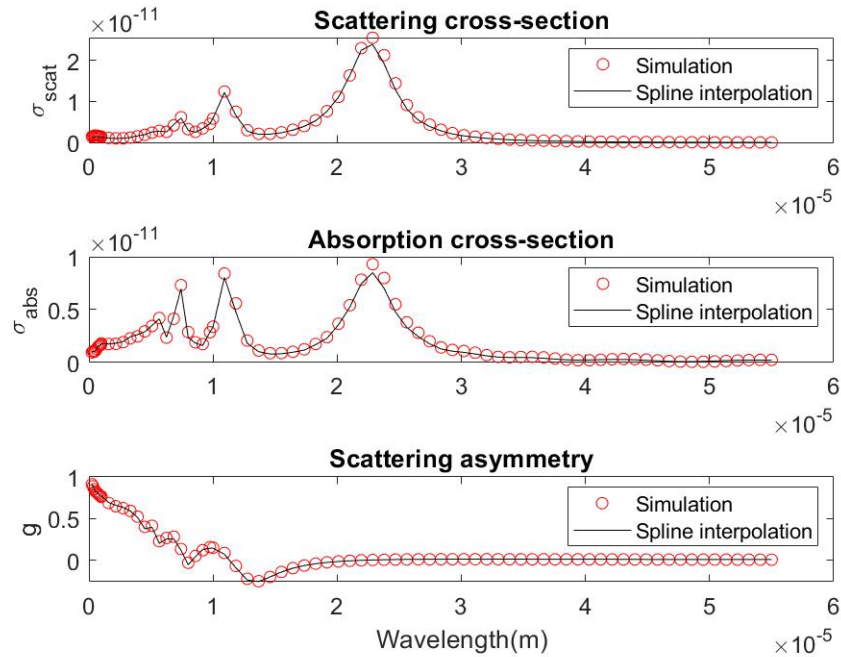


**Fig. S4.** FDTD output figure, showing orientation dependence of the optical properties of a 9  $\mu\text{m}$ -long,  $\sim 60:1$  aspect ratio Fe nanorod. (a) Cross-sections as a function of wavelength. (b) Cross-sections and scattering asymmetry as a function of orientation for wavelengths 21.9  $\mu\text{m}$  (solid lines, bold labels) and 0.70  $\mu\text{m}$  (dashed lines, italic labels).

Results of interpolation and simulation at  $\phi=15, \theta=15$



Results of interpolation and simulation at  $\phi=60, \theta=15$



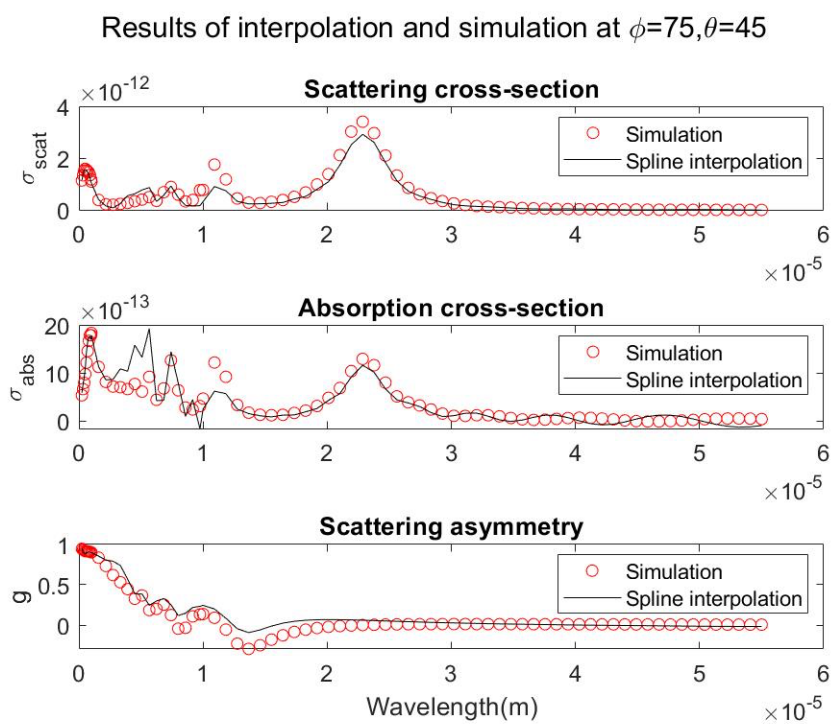
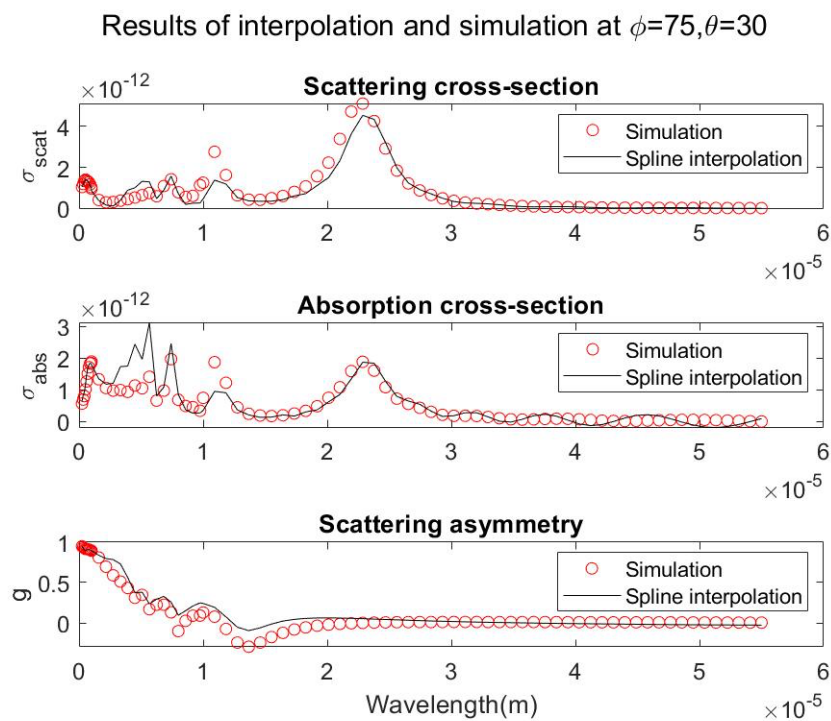


**Fig. S5.** Results of interpolation check. 9  $\mu\text{m}$ -long,  $\sim 60:1$  aspect ratio Fe nanorod. Units of angles are degrees.

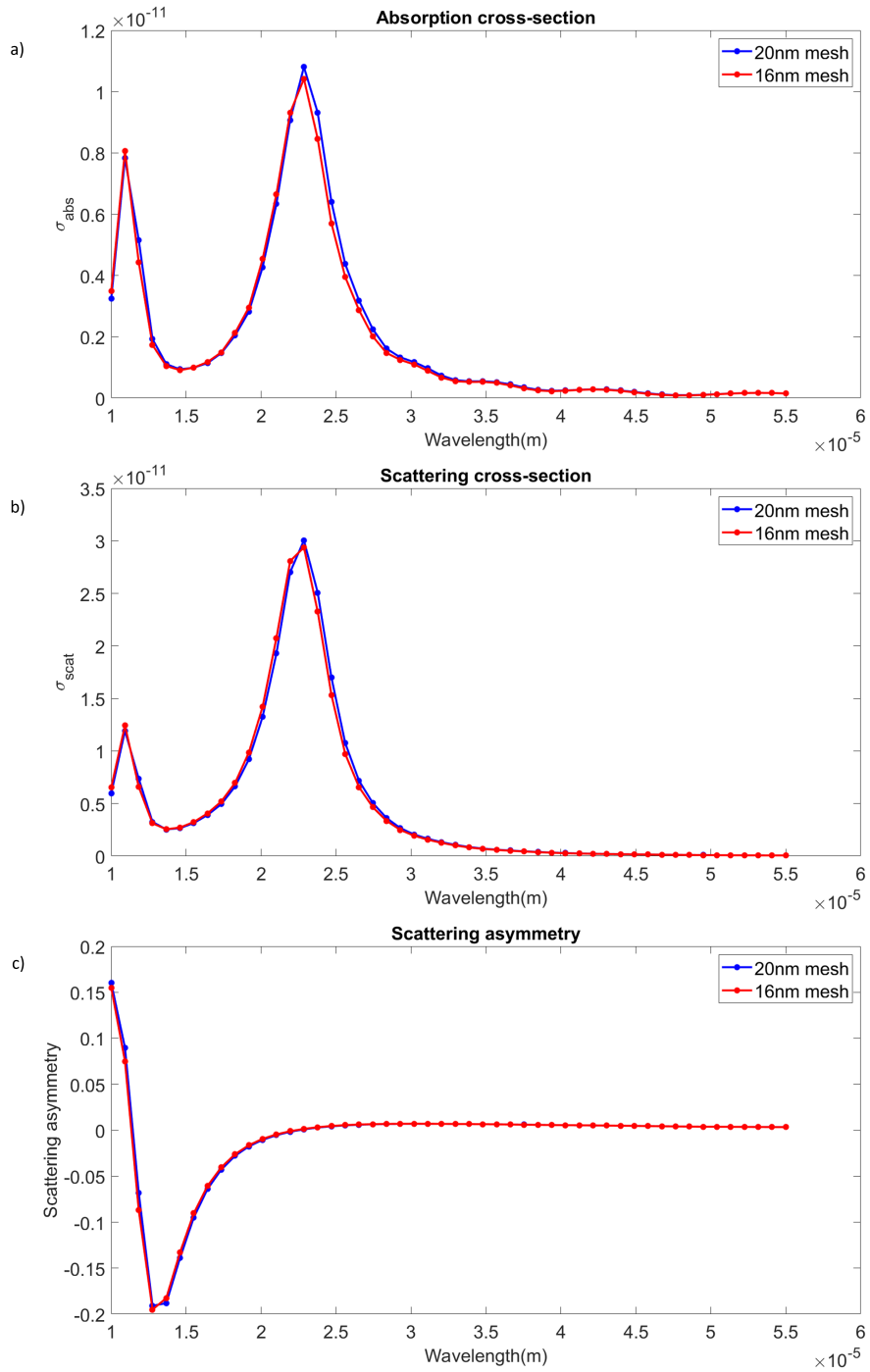


**Fig. S6.** Sensitivity test showing change in optical properties when mesh resolution is increased (decreasing mesh spacing). 9  $\mu\text{m}$ -long,  $\sim 60:1$  aspect ratio Fe nanorod. Orientation:  $\theta = 45^\circ$ ,  $\varphi = 45^\circ$ .

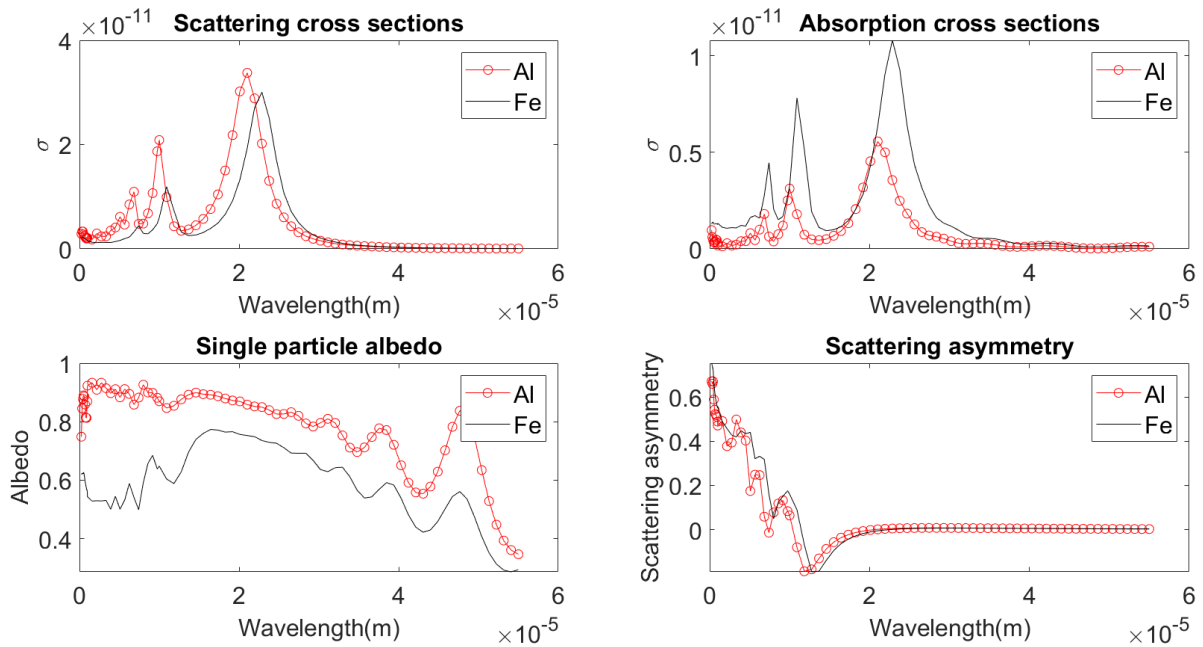


**Fig. S7.** Showing sensitivity of calculated optical properties to changing nanorod composition (Al vs. Fe), for a 9  $\mu\text{m}$ -long,  $\sim 60:1$  aspect ratio nanorod. The total extinction cross section (scattering plus absorption) and the location of the resonances remains about the same; a small increase in Al nanorod length would be sufficient to closely match the Fe cross-sections. As Al is  $3\times$  less dense than Fe, this suggests Al is more effective on a warming-per-unit-mass basis. Conductive-nanorod size and shape, and not composition, are the main controls on simulated nanorod optical properties. Aluminum material properties are obtained from ref. 51. Orientation:  $\theta = 45^\circ$ ,  $\varphi = 45^\circ$ .

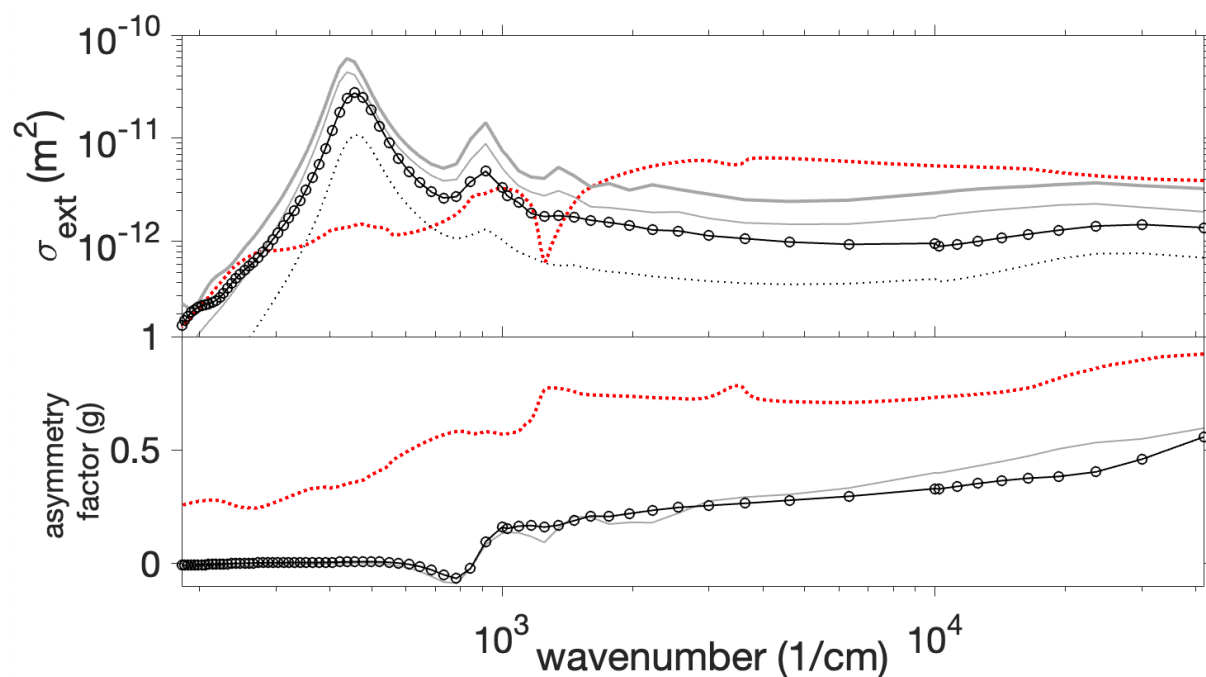


**Fig. S8.** Showing the calculated optical properties varying particle length and width for the same particle composition: specifically, 7.5  $\mu\text{m}$ -long Fe nanorods with cross-section  $0.08 \mu\text{m} \times 0.08 \mu\text{m}$ , compared to 9  $\mu\text{m}$ -long Fe nanorods with cross-section  $0.16 \mu\text{m} \times 0.16 \mu\text{m}$ . Orientation-averaged optical properties calculated using a 3D Finite-Difference Time-Domain (FDTD) approach. Upper panel: Solid black line corresponds to total extinction, dotted black line to scattering, both for 7.5  $\mu\text{m}$ -long Fe nanorods with cross-section  $0.08 \mu\text{m} \times 0.08 \mu\text{m}$ . Lower panel shows scattering asymmetry. Also shown in both panels are spectra for natural dust assuming a log-gaussian particle size distribution centered on 2.5  $\mu\text{m}$  (48) (red dotted lines). In both panels, gray lines correspond to the results for a 9  $\mu\text{m}$ -long Fe nanorod with cross-section  $0.16 \mu\text{m} \times 0.16 \mu\text{m}$ . As expected given its spectrum, the 7.5  $\mu\text{m}$ -long nanorod gives  $\sim 2\times$  less warming per nanorod in climate simulations. However, as it uses  $5\times$  less Fe, this design is more effective on a warming-per-unit-mass basis.

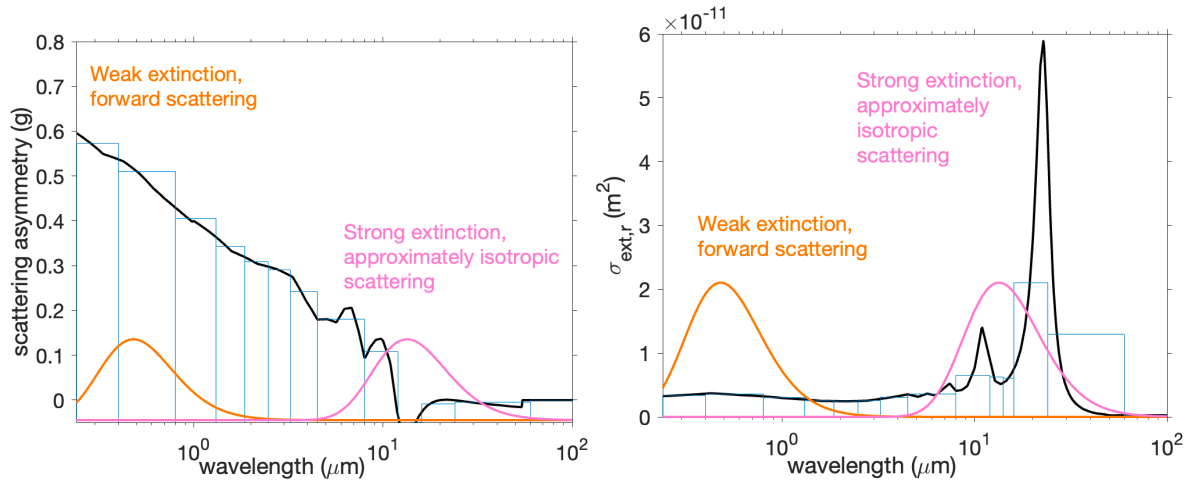


**Fig. S9.** Showing how the spectra are represented within the 3-D climate model. 9 μm-long, ~60:1 aspect ratio nanorod. 4.5 μm marks the separation between solar bins (Planck-weighted using the orange 6000 K blackbody curve, normalized W/m<sup>2</sup>/μm flux density), and thermal IR bins (Planck-weighted using the pink 215 K blackbody curve, normalized W/m<sup>2</sup>/μm flux density). The relative heights of the orange and pink Planck functions are to guide the eye only and have no physical significance.

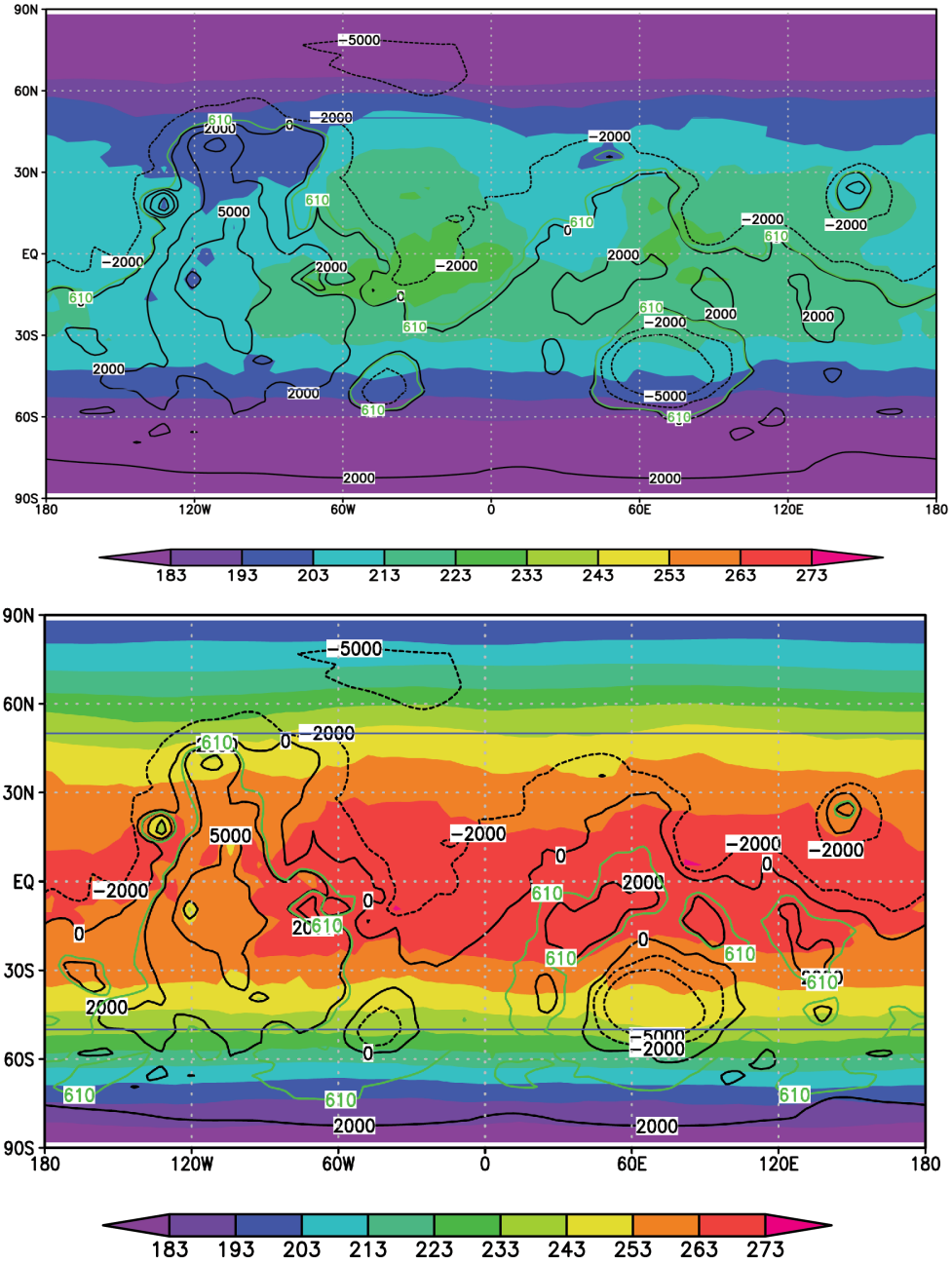


**Fig. S10.** Annual average temperatures (K) for (top) control simulation without nanorods (i.e., Fig. 2b), and (bottom) warmed case with  $\sim 160 \text{ mg/m}^2$  Al nanorods (i.e., Fig. 2a). Labeled black contours correspond to topographic elevation in m. Green contour corresponds to 610 Pa ( $\sim 6$  mbar) mean pressure level. Blue lines: approximate latitudinal (equatorward) extent of ice at  $<1$  m depths.

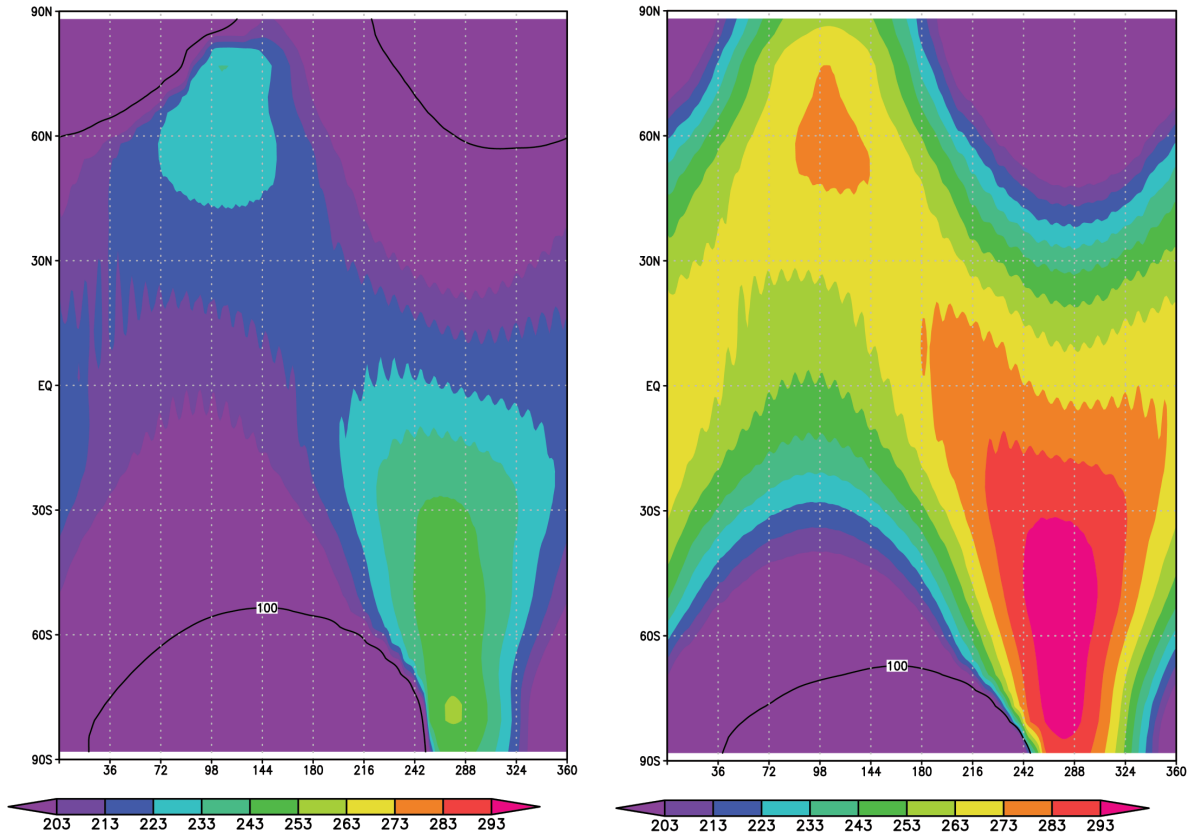


**Fig. S11.** Seasonal variation of diurnal-average surface temperature (K) for (left) control simulation without nanorods (i.e., Fig. 2b), and (right) warmed case with  $\sim 160 \text{ mg/m}^2$  nanorods (i.e., Fig. 2a), showing longitudinal average surface temperature. Each of the 10 increments on the x-axis, which are equally spaced in time, corresponds to 1/10 of a Mars year (69 Earth days). To make this figure, a 9-point smoother has been used (3 points in time, and 3 points in latitude) in order to damp oscillations associated with aliasing in the sampling of the day-night temperature cycle in the output. The black lines show the limit of substantial polar seasonal CO<sub>2</sub> ice.

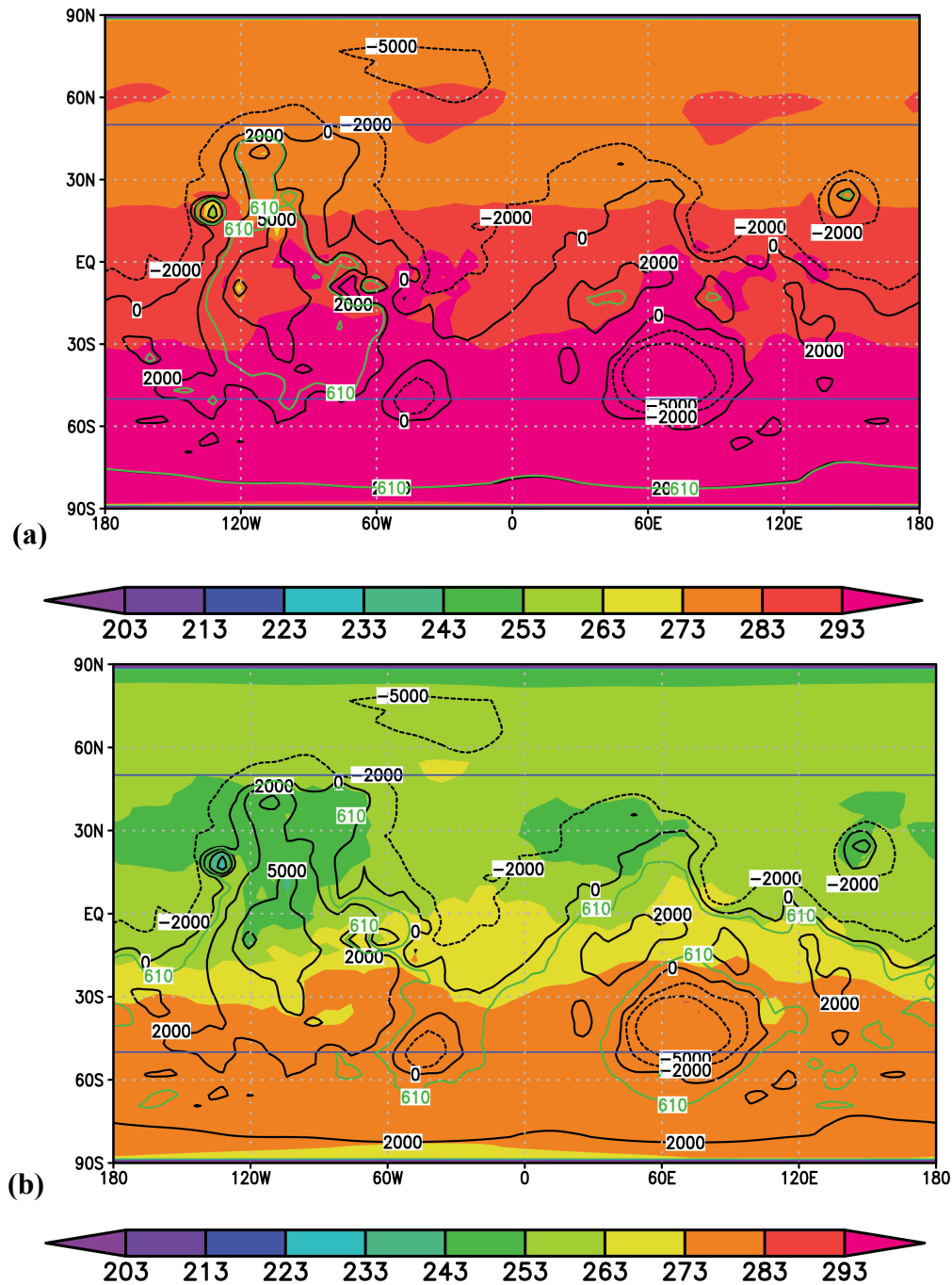


**Fig. S12.** Sensitivity tests showing how warm-season temperatures vary for different parameter choices. Baseline is Fe nanorod results shown in Fig. S19. Labeled black contours correspond to topographic elevation in m. Green contour corresponds to 610 Pa ( $\sim 6$  mbar) mean pressure level. Blue lines: approximate latitudinal (equatorward) extent of ice at <1 m depths. (a) More nanorods ( $\tau_{Fe} = 1.5$ ): the average surface pressure exceeds 610 Pa (green contour) at all locations below +2 km elevation. (b) Fewer nanorods ( $\tau_{Fe} = 0.375$ ).

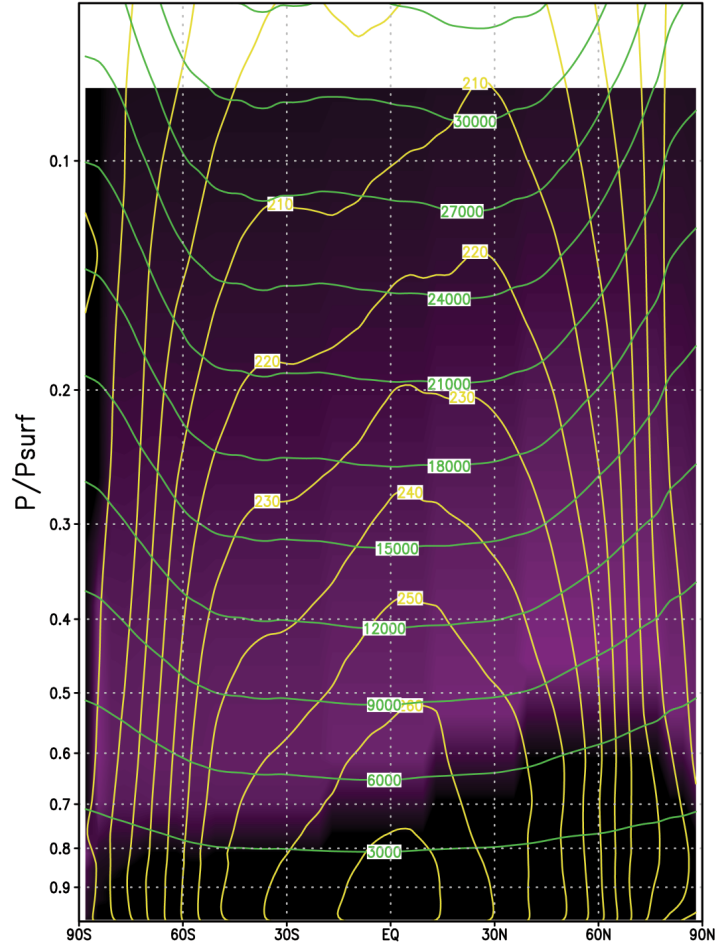


**Fig. S13.** Cross section of steady (imposed) nanorod layer ( $\tau_{Fe} = 0.75$ , Fig. S19). The purple shading corresponds to the relative volume density of nanorods. The mixing ratio of nanorods within the purple layer is uniform, but there is more gas closer to the planet's surface so there are also more nanorods lower down. The tenuous part of the nanorod layer extending to high altitude is disproportionately important because of its strong contribution to the greenhouse effect. The Y-axis uses terrain-following  $\eta$ -coordinates ( $\eta = P/P_{surf}$ , where the model-top pressure has been subtracted from both pressures), and the cloud lines are tilted down and to the left because the southern hemisphere surface is topographically higher and thus closer to the fixed-pressure base of the nanorod layer. The yellow lines are contours of annual average atmospheric temperature. The green lines are contours of altitude in meters, which bow upwards at the poles where low temperatures compact the gas column.

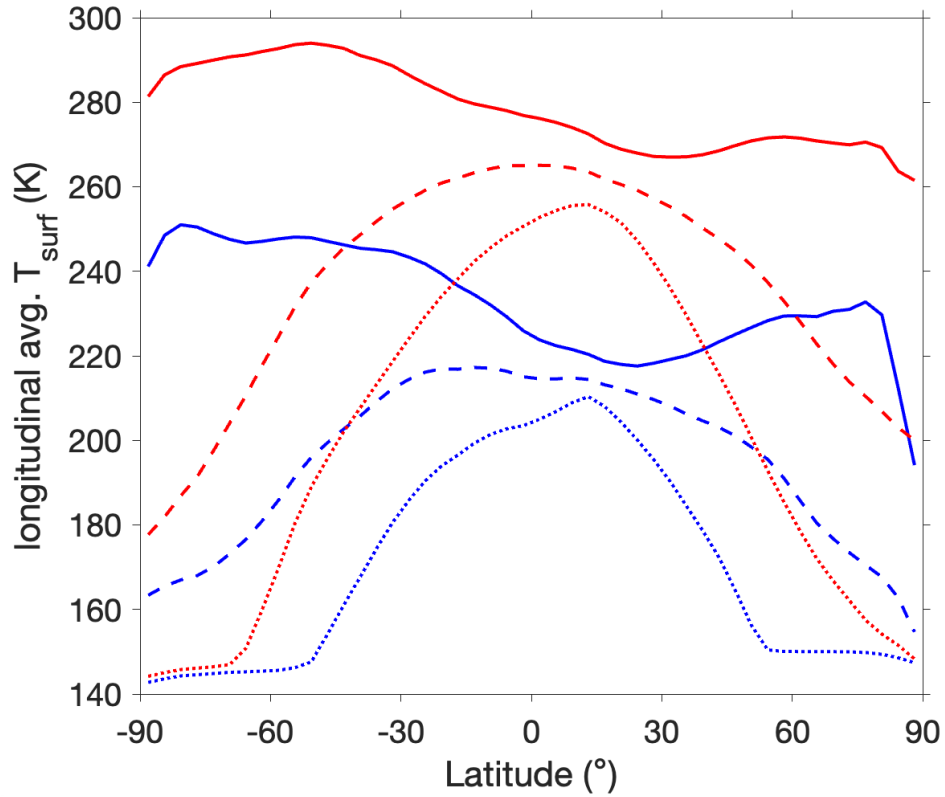


**Fig. S14.** Summary of the latitudinal and seasonal dependence of surface temperature for (red lines) the 3D model with-nanorods  $\tau_{Fc} = 0.75$  case (Fig. S19a), and (blue lines) the 3D model without nanorods (Fig. S19b). Solid line corresponds to the average temperature during the warmest season ( $\sim 70$  day period) during the year, dotted line corresponds to the average temperature during the coldest season ( $\sim 70$  day period) of the year, and dashed line corresponds to the annual average. The flattening-out of the lines around 145 K corresponds to buffering at the frost point of  $\text{CO}_2$ .

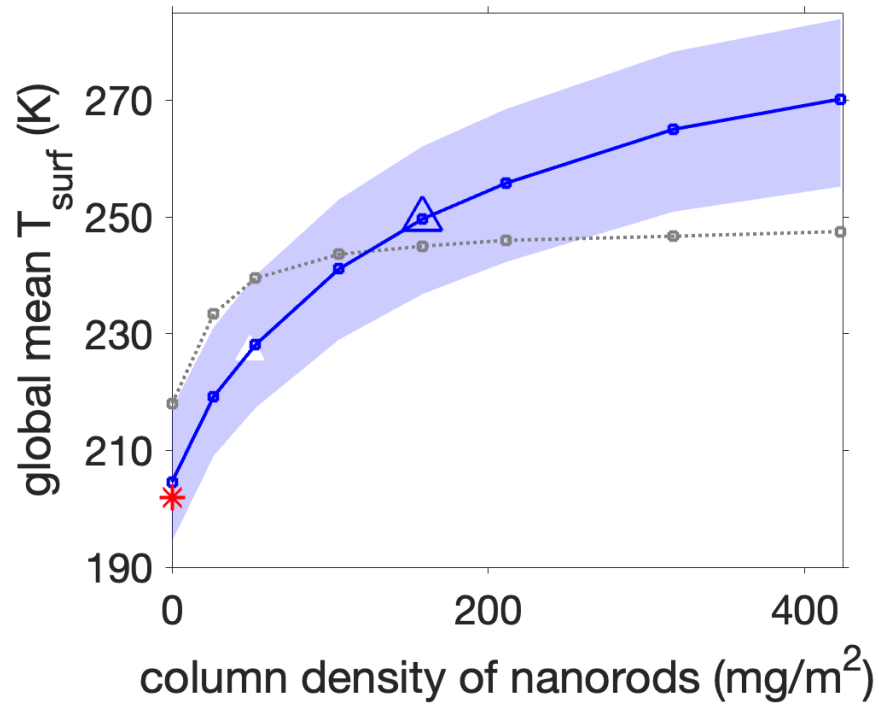


**Fig. S15.** As Fig 2c, but with a linear x-axis instead of a logarithmic x-axis. Dependence of planet-averaged surface warming on nanorod column mass. Blue triangle corresponds to Fig. 2a, the intersection of the blue line with the zero-nanorods axis corresponds to Fig. 2b, and white triangle marks onset of warm-season temperatures above the freezing point of water at 50°S. Blue corresponds to 3-D results. The blue envelope corresponds to the modeled seasonal range in global mean  $T_{surf}$ . Gray corresponds to 1-D results. The red asterisk corresponds to the observed modern Mars value.

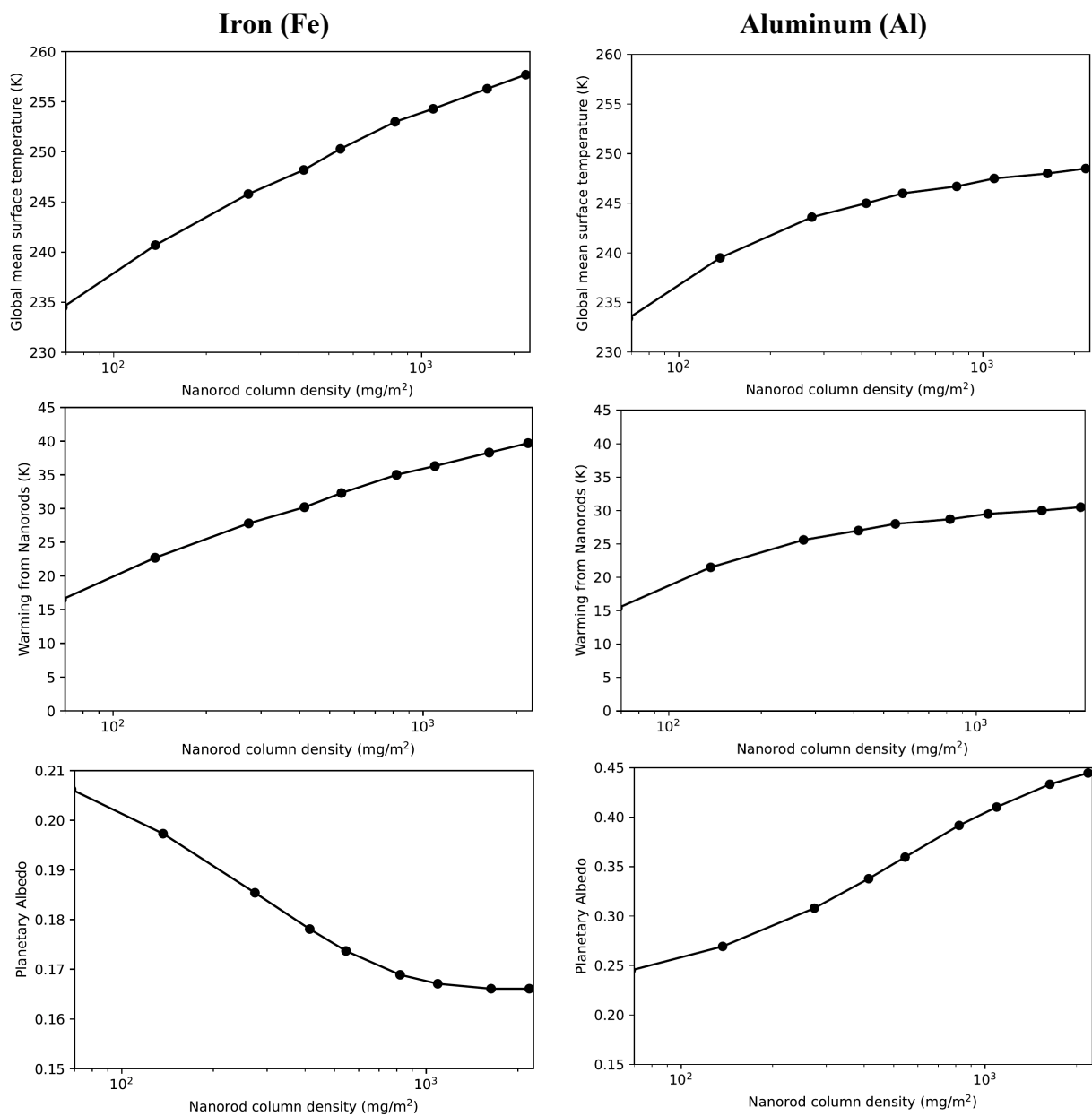


**Fig. S16.** Summary of 1-D climate model output as a function of nanorod column density. Left column corresponds to Fe, right column corresponds to Al.

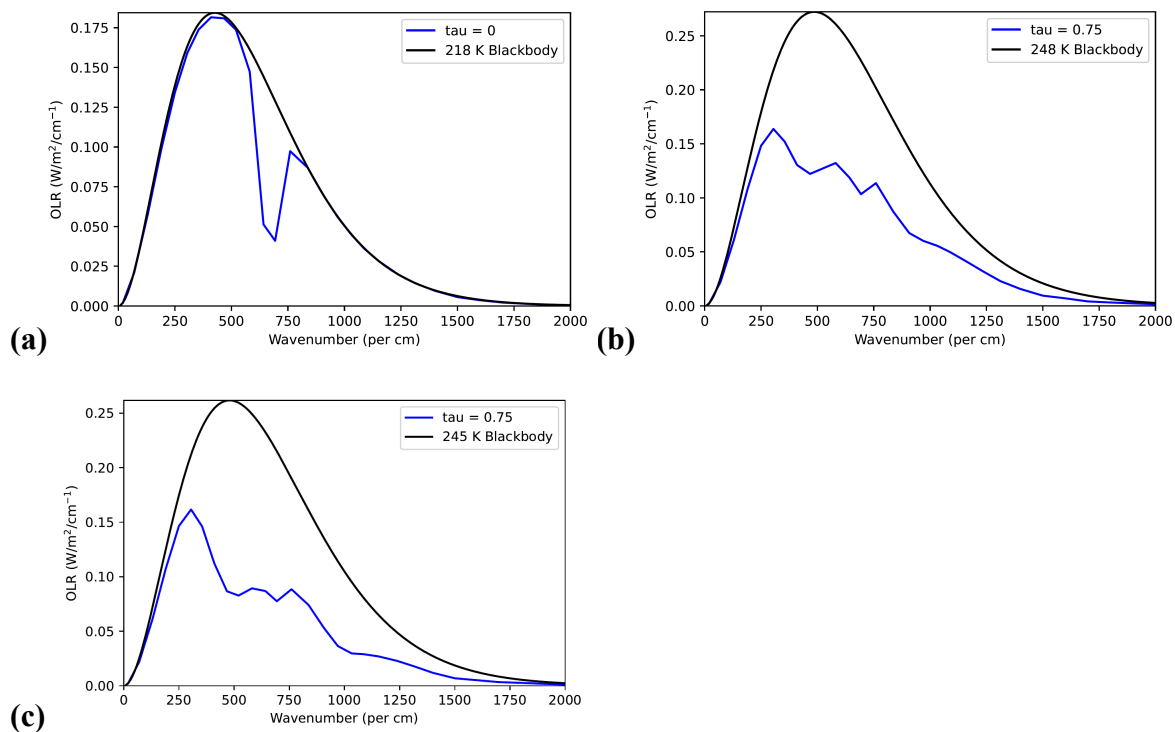


**Fig. S17.** Outgoing Longwave Radiation (OLR) from the 1D model. The integrated top-of-atmosphere OLR values are  $\sim 114.6$ ,  $96.6$ , and  $120 \text{ W/m}^2$  for the no-nanorod, Al and Fe nanorod cases, respectively. **(a)** The no-nanorods case. Spectral windows are visible as peaks on either side of the  $\text{CO}_2$  band which is at 600-800  $\text{per cm}$ . **(b)** The nanorods case with  $\tau_{\text{Fe}} = 0.75$ . Absence of prominent peaks corresponds to closure of the spectral windows. **(c)** The nanorods case with  $\tau_{\text{Al}} = 0.75$ .

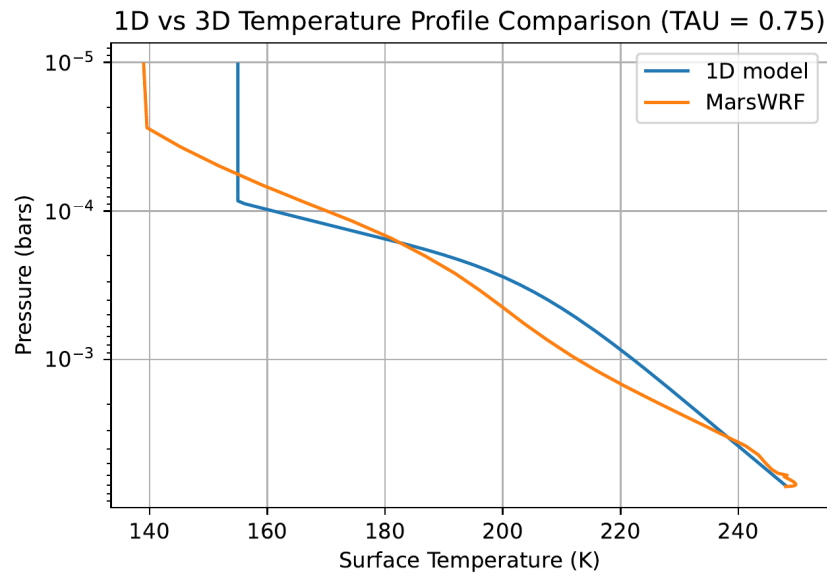


**Fig. S18.** 1D model vs. 3D (MarsWRF) model temperature profile comparison for  $\tau_{\text{Fe}} = 0.75$ . The 3D result is the global and annual average. At this optical depth, surface temperature for both models is  $\sim 250$  K.

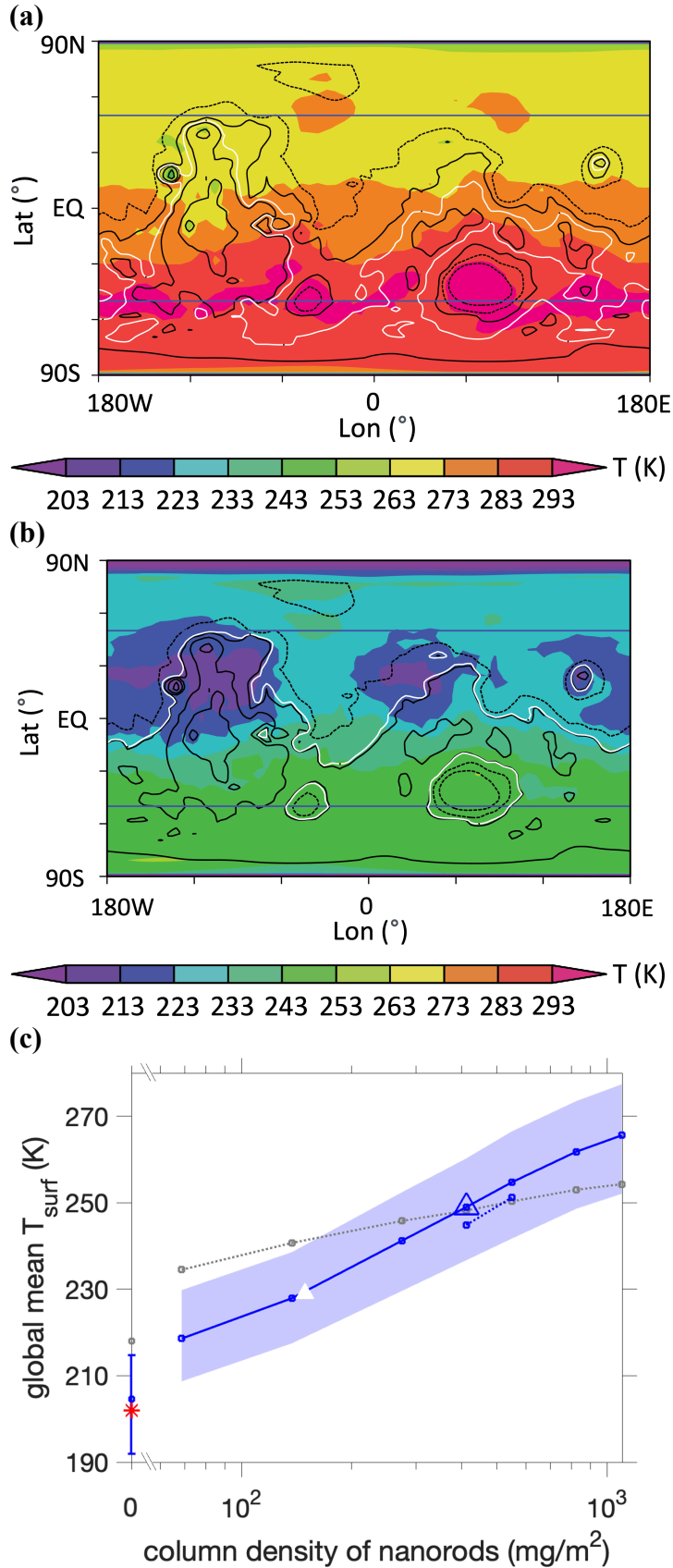


**Fig. S19.** As Fig. 2, but for 400  $\text{mg/m}^2$  loading of Fe nanorods instead of 160  $\text{mg/m}^2$  loading of Al nanorods. Warm-season temperatures (K) (color shading) on (a) Mars with addition of  $\sim 400 \text{ mg/m}^2$  of nanorods, (b) control case. This corresponds to the average surface temperature during the warmest  $36^\circ$  of solar longitude ( $\sim 70$  days) of the year. White contour corresponds to 610 Pa ( $\sim 6$  mbar) mean pressure level. Black contours correspond to topographic elevation in m (dashed:  $-5$  km and  $-2$  km, solid: 0 km,  $+2$  km, and  $+5$  km). Blue lines: approximate latitudinal (equatorward) extent of ice at  $<1$  m depths. Results do not include  $\text{CO}_2$  outgassing from within polar ice, which would cause further warming. (c) Dependence of planet-averaged surface warming on nanorod column mass. Blue line corresponds to 3-D results, varying layer-top height between  $\sim 35$  km (solid line) and  $\sim 28$  km (dashed line). The blue envelope corresponds to the modeled seasonal range in global mean  $T_{surf}$ . Gray corresponds to 1-D results (see text for details). Blue triangle corresponds to panel (a), and white triangle marks onset of warm-season temperatures above the freezing point of water at  $50^\circ\text{S}$ . Symbols on y-axis are temperatures for the no-nanorod case, with the red asterisk corresponding to observed Mars value. More detail is shown in Figs. S10-S17.

Material	Iron (Fe)			Aluminum (Al)		
	wavelength ( $\times 10^{-4}$ m)	absorption cross-section ( $\times 10^{-10}$ m <sup>2</sup> )	scattering cross-section ( $\times 10^{-10}$ m <sup>2</sup> )	asymmetry parameter (g)	absorption cross-section ( $\times 10^{-10}$ m <sup>2</sup> )	scattering cross-section ( $\times 10^{-10}$ m <sup>2</sup> )
0.0024	0.0131	0.0194	0.596	0.0114	0.0236	0.5204
0.0033	0.0133	0.0215	0.549	0.0053	0.0325	0.4205
0.0043	0.0138	0.0232	0.5327	0.0044	0.0351	0.4454
0.0052	0.0131	0.0226	0.505	0.0036	0.0298	0.4093
0.0061	0.0128	0.0214	0.4728	0.0034	0.0274	0.3687
0.007	0.0128	0.0205	0.4492	0.0037	0.0254	0.3548
0.008	0.0127	0.0196	0.4301	0.0045	0.0233	0.3536
0.0089	0.0125	0.0186	0.4131	0.0044	0.0220	0.3450
0.0098	0.0121	0.0177	0.3979	0.0028	0.0216	0.3350
0.01	0.0125	0.017	0.3997	0.0012	0.0221	0.3178
0.0158	0.0104	0.0148	0.3322	0.0011	0.0213	0.2824
0.0217	0.0098	0.0147	0.3041	0.0022	0.0274	0.2659
0.0275	0.0102	0.0152	0.2921	0.0032	0.0349	0.2400
0.0333	0.012	0.0168	0.2745	0.0048	0.0441	0.0693
0.0392	0.0127	0.0193	0.2218	0.0068	0.0562	0.0755
0.045	0.0163	0.0191	0.1798	0.0027	0.0303	0.1405
0.0508	0.0112	0.0203	0.1804	0.0043	0.0394	0.1514
0.0567	0.0152	0.0213	0.1732	0.0025	0.0377	0.1627
0.0625	0.012	0.0217	0.2035	0.0054	0.0532	0.1700
0.0683	0.0163	0.0271	0.206	0.0073	0.0588	0.0671
0.0742	0.0214	0.031	0.1553	0.0044	0.0443	0.0308
0.08	0.013	0.0278	0.0922	0.0046	0.0508	0.0664
0.0858	0.012	0.0302	0.119	0.0053	0.0650	0.0825
0.0917	0.0138	0.0347	0.1344	0.0101	0.0916	0.0818
0.0975	0.0225	0.0452	0.1368	0.0182	0.1456	0.0490
0.1	0.0247	0.0514	0.1327	0.0223	0.1579	0.0321
0.1092	0.0532	0.0886	0.0835	0.0130	0.0854	-0.0657
0.1184	0.0359	0.0619	-0.0233	0.0066	0.0549	-0.1176
0.1276	0.0165	0.0399	-0.0872	0.0057	0.0551	-0.1074
0.1367	0.0125	0.0387	-0.0822	0.0064	0.0630	-0.0808
0.1459	0.0126	0.0437	-0.057	0.0080	0.0768	-0.0579
0.1551	0.0145	0.0524	-0.0352	0.0107	0.0976	-0.0427
0.1643	0.0178	0.0644	-0.0205	0.0146	0.1274	-0.0337
0.1735	0.0234	0.0813	-0.0109	0.0215	0.1720	-0.0284
0.1827	0.032	0.1081	-0.0053	0.0327	0.2449	-0.0254
0.1918	0.0451	0.1489	-0.0018	0.0501	0.3503	-0.0240

0.201	0.067	0.2132	-0.0001	0.0700	0.4696	-0.0235
0.2102	0.0987	0.3056	0.0006	0.0818	0.5050	-0.0235
0.2194	0.1371	0.4119	0.0007	0.0707	0.4157	-0.0240
0.2286	0.1553	0.4378	0.0003	0.0501	0.2839	-0.0246
0.2378	0.1293	0.3514	-0.0004	0.0349	0.1829	-0.0252
0.2469	0.0886	0.2335	-0.0011	0.0246	0.1214	-0.0259
0.2561	0.0604	0.1484	-0.0019	0.0169	0.0840	-0.0268
0.2653	0.0428	0.099	-0.0028	0.0124	0.0599	-0.0276
0.2745	0.0304	0.0691	-0.0037	0.0101	0.0443	-0.0283
0.2837	0.0228	0.0495	-0.0044	0.0082	0.0340	-0.0289
0.2929	0.0186	0.0369	-0.0051	0.0065	0.0267	-0.0296
0.302	0.0154	0.0285	-0.0059	0.0053	0.0213	-0.0303
0.3112	0.0124	0.0224	-0.0066	0.0047	0.0172	-0.0309
0.3204	0.0103	0.0179	-0.0072	0.0042	0.0141	-0.0314
0.3296	0.0089	0.0145	-0.0077	0.0038	0.0117	-0.0318
0.3388	0.008	0.0119	-0.0081	0.0033	0.0098	-0.0321
0.348	0.007	0.0099	-0.0085	0.0028	0.0083	-0.0325
0.3571	0.0061	0.0084	-0.009	0.0026	0.0071	-0.0329
0.3663	0.0054	0.0071	-0.0095	0.0024	0.0061	-0.0332
0.3755	0.0049	0.0061	-0.01	0.0022	0.0053	-0.0335
0.3847	0.0045	0.0052	-0.0104	0.0020	0.0046	-0.0338
0.3939	0.0041	0.0046	-0.0108	0.0017	0.0040	-0.0340
0.4031	0.0036	0.004	-0.0112	0.0015	0.0036	-0.0342
0.4122	0.0032	0.0035	-0.0115	0.0014	0.0032	-0.0343
0.4214	0.0029	0.0031	-0.0119	0.0013	0.0028	-0.0345
0.4306	0.0027	0.0028	-0.0123	0.0014	0.0025	-0.0348
0.4398	0.0027	0.0025	-0.0127	0.0014	0.0023	-0.0350
0.449	0.0027	0.0022	-0.0132	0.0014	0.0021	-0.0352
0.4582	0.0026	0.002	-0.0136	0.0013	0.0019	-0.0353
0.4673	0.0024	0.0018	-0.0139	0.0011	0.0017	-0.0355
0.4765	0.0021	0.0017	-0.0143	0.0009	0.0016	-0.0356
0.4857	0.0018	0.0015	-0.0146	0.0007	0.0014	-0.0358
0.4949	0.0015	0.0014	-0.0149	0.0005	0.0013	-0.0359
0.5041	0.0013	0.0012	-0.0151	0.0003	0.0012	-0.0359
0.5133	0.0012	0.0011	-0.0153	0.0003	0.0011	-0.0360
0.5224	0.0012	0.001	-0.0155	0.0004	0.0010	-0.0361
0.5316	0.0013	0.0009	-0.0156	0.0006	0.0009	-0.0361
0.5408	0.0015	0.0009	-0.0158	0.0008	0.0008	-0.0362
0.55	0.0017	0.0008	-0.016	0.0010	0.0008	-0.0363

**Supplementary Table 1:** Orientation-averaged optical properties of nanorods as used in the climate simulations, corresponding to a 9  $\mu\text{m}$ -long nanorod with cross-section (0.16 $\times$ 0.16)  $\mu\text{m}$ .

Optical depth ( $\tau$ ) at $\lambda = 0.67 \mu\text{m}$	Nanorod column mass ( $\text{mg}/\text{m}^2$ )	1-D temperature output, global mean (K)	3D temperature output		
			3-D global mean temperature (K)	50°N warm-season temperature (K)	50°S warm-season temperature (K)
0	0	218.0	204.6	228.8	250.3
0.125 (Al)	26.6	233.4	219.2	243.2	264.3
0.25 (Al)	53.2	239.5	228.1	253.0	274.4
0.5 (Al)	106.5	243.6	241.1	265.8	289.0
0.75 (Al)	161.2	245.0	249.7	274.3	298.2
1 (Al)	212.1	246.0	255.8	280.2	304.8
1.5 (Al)	319.4	246.7	265.0	287.6	312.3
2 (Al)	424.6	247.5	270.3	291.6	316.7
0.125 (Fe)	68.4	234.5	218.6	241.2	262.2
0.25 (Fe)	136.6	240.7	227.9	250.9	271.9
0.5 (Fe)	273.8	245.8	241.2	263.2	285.9
0.75 (Fe)	414.3	248.2	249.0	270.9	294.0
1 (Fe)	545.1	250.3	254.7	275.7	299.3
1.5 (Fe)	820.8	253.0	261.8	281.5	304.9
2 (Fe)	1091.1	254.3	265.6	285.0	307.1

**Supplementary Table 2.** Summary of climate model output. The nanorod column mass differs between the Al and Fe cases by a factor of 2.57 (ratio of material densities, corrected for the 13% greater extinction cross-section of Fe rods at  $0.67 \mu\text{m}$  relative to Al rods).

Description	Optical depth ( $\tau$ ) at $\lambda = 0.67 \mu\text{m}$	3D temperature output		
		3-D global mean temperature (K)	50°N warm-season temperature (K)	50°S warm-season temperature (K)
<i>Reference</i>	0.75	249.0	270.9	294.0
Lower cloud top (~28 km vs. ~35 km)	0.75	244.8	270.6	289.5
Lower cloud top (~28 km vs. ~35 km)	1	251.2	275.6	297.1
2× atmospheric pressure ( $\approx 12$ mbar)	0.75	252.7	269.9	290.1
Nanorods extend only from 45°S - 45°N	0.75	237.7	230.5	253.2
Nanorods only active from $L_s = 180 - 360$ , passive at other seasons	0.75	224.9	229.2	293.3
5× greater output frequency	0.75	249.0	270.8	294.0
2× smaller numerical timestep	0.75	249.5	271.0	293.5
Thinner cloud (200 Pa base, 8 levels)	0.75	248.7	269.3	290.9
96×72 spatial grid in model (vs. default of 64×48)	0.75	250.5	271.1	292.9

**Supplementary Table 3.** Summary output for additional sensitivity tests using 3D model. All were carried out using Fe nanorods.

## REFERENCES AND NOTES

1. N. Mangold, S. Gupta, O. Gasnault, G. Dromart, J. D. Tarnas, S. F. Sholes, B. Horgan, C. Quantin-Nataf, A. J. Brown, S. le Mouélic, R. A. Yingst, J. F. Bell, O. Beyssac, T. Bosak, F. Calef III, B. L. Ehlmann, K. A. Farley, J. P. Grotzinger, K. Hickman-Lewis, S. Holm-Alwmark, L. C. Kah, J. Martinez-Frias, S. McLennan, S. Maurice, J. I. Nuñez, A. M. Ollila, P. Pilleri, Rice JW Jr, M. Rice, J. I. Simon, D. L. Shuster, K. M. Stack, V. Z. Sun, A. H. Treiman, B. P. Weiss, R. C. Wiens, A. J. Williams, N. R. Williams, K. H. Williford, Perseverance rover reveals an ancient delta-lake system and flood deposits at Jezero crater, Mars. *Science* **374**, 711–717 (2021).
2. J. P. Grotzinger, D. Y. Sumner, L. C. Kah, K. Stack, S. Gupta, L. Edgar, D. Rubin, K. Lewis, J. Schieber, N. Mangold, R. Milliken, P. G. Conrad, D. D. Marais, J. Farmer, K. Siebach, F. Calef III, J. Hurowitz, S. M. Mc Lennan, D. Ming, D. Vaniman, J. Crisp, A. Vasavada, K. S. Edgett, M. Malin, D. Blake, R. Gellert, P. Mahaffy, R. C. Wiens, S. Maurice, J. A. Grant, S. Wilson, R. C. Anderson, L. Beegle, R. Arvidson, B. Hallet, R. S. Sletten, M. Rice, J. Bell III, J. Griffes, B. Ehlmann, R. B. Anderson, T. F. Bristow, W. E. Dietrich, G. Dromart, J. Eigenbrode, A. Fraeman, C. Hardgrove, K. Herkenhoff, L. Jandura, G. Kocurek, S. Lee, L. A. Leshin, R. Leveille, D. Limonadi, J. Maki, S. M. Closkey, M. Meyer, M. Minitti, H. Newsom, D. Oehler, A. Okon, M. Palucis, T. Parker, S. Rowland, M. Schmidt, S. Squyres, A. Steele, E. Stolper, R. Summons, A. Treiman, R. Williams, A. Yingst, A habitable fluvio-lacustrine environment at Yellowknife Bay, Gale Crater Mars. *Science* **343**, 1242777 (2014).
3. W. C. Feldman, T. H. Prettyman, S. Maurice, J. J. Plaut, D. L. Bish, D. T. Vaniman, M. T. Mellon, A. E. Metzger, S. W. Squyres, S. Karunatillake, W. V. Boynton, R. C. Elphic, H. O.

- Funsten, D. J. Lawrence, R. L. Tokar, Global distribution of near-surface hydrogen on Mars. *J. Geophys. Res. Planets* **109**, doi.org/10.1029/2003JE002160 (2004).
4. C. M. Dundas, A. M. Bramson, L. Ojha, J. J. Wray, M. T. Mellon, S. Byrne, Alfred S. McEwen, N. E. Putzig, D. Viola, S. Sutton, E. Clark, J. W. Holt, Exposed subsurface ice sheets in the Martian mid-latitudes. *Science* **359**, 199–201 (2018).
5. C. P. McKay, Requirements and limits for life in the context of exoplanets. *Proc. Natl. Acad. Sci. U.S.A.* **111**, 12628–12633 (2014).
6. J. L. Dickson, A. M. Palumbo, J. W. Head, L. Kerber, C. I. Fassett, M. A. Kreslavsky, Gullies on Mars could have formed by melting of water ice during periods of high obliquity. *Science* **380**, 1363–1367 (2023).
7. C. P. McKay, O. B. Toon, J. F. Kasting, Making Mars habitable. *Nature* **352**, 489–496 (1991).
8. M. M. Marinova, C. P. McKay, H. Hashimoto, Radiative-convective model of warming Mars with artificial greenhouse gases. *J. Geophys. Res. Planets* **110**, <https://doi.org/10.1029/2004JE002306> (2005).
9. R. Wordsworth, L. Kerber, C. Cockell, Enabling Martian habitability with silica aerogel via the solid-state greenhouse effect. *Nat. Astron.* **3**, 898–903 (2019).
10. R. M. Haberle, Estimating the power of Mars' greenhouse effect. *Icarus* **223**, 619–620 (2013).
11. B. M. Jakosky, C. S. Edwards. Inventory of CO<sub>2</sub> available for terraforming Mars. *Nat. Astron.* **2**, 634–639 (2018).
12. M. F. Gerstell, J. S. Francisco, Y. L. Yung, C. Boxe, E. T. Aaltonen, Keeping Mars warm with new super greenhouse gases. *Proc. Natl. Acad. Sci. U.S.A.* **98**, 2154–2157 (2001).

13. E. S. Kite, D. P. Mayer, Mars sedimentary rock erosion rates constrained using crater counts, with applications to organic-matter preservation and to the global dust cycle. *Icarus* **286**, 212–222 (2017).
14. D. J. McCleese, N. G. Heavens, J. T. Schofield, W. A. Abdou, J. L. Bandfield, S. B. Calcutt, P. G. J. Irwin, D. M. Kass, A. Kleinböhl, S. R. Lewis, D. A. Paige, P. L. Read, M. I. Richardson, J. H. Shirley, F. W. Taylor, N. Teanby, R. W. Zurek, Structure and dynamics of the Martian lower and middle atmosphere as observed by the Mars Climate Sounder: Seasonal variations in zonal mean temperature, dust, and water ice aerosols. *J. Geophys. Res. Planets* **115**, <https://doi.org/10.1029/2010JE003677> (2010).
15. M. A. Kahre, J. R. Murphy, C. E. Newman, R. J. Wilson, B. A. Cantor, M. T. Lemmon, M. J. Wolff, “The Mars dust cycle” in *The Atmosphere and Climate of Mars*, R. Haberle, Ed. (Cambridge Univ. Press, 2017), pp. 295.
16. P. M. Streeter, S. R. Lewis, M. R. Patel, J. A. Holmes, D. M. Kass, Surface warming during the 2018/Mars year 34 global dust storm. *Geophys. Res. Lett.* **47**, e2019GL083936 (2020).
17. J. H. Van Vleck, F. Bloch, M. Hammesh, Theory of radar reflection from wires or thin metallic strips. *J. Appl. Phys.* **18**, 274–294 (1947).
18. J. Seinfeld, S. Pandis, Atmospheric chemistry and physics (Wiley, ed. 3, 2016).
19. F. Forget, R. T. Pierrehumbert, Warming early Mars with carbon dioxide clouds that scatter infrared radiation. *Science* **278**, 1273–1276 (1997).
20. M. I. Richardson, A. D. Toigo, C. E. Newman, PlanetWRF: A general purpose, local to global numerical model for planetary atmospheric and climate dynamics. *J. Geophys. Res. Planets* **112**, E09001 (2007).

21. A. D. Toigo, C. Lee, C. E. Newman, M. I. Richardson, The impact of resolution on the dynamics of the martian global atmosphere: Varying resolution studies with the MarsWRF GCM. *Icarus* **221**, 276–288 (2012).
22. E. S. Kite, L. J. Steele, M. A. Mischna, M. I. Richardson, Warm early Mars surface enabled by high-altitude water ice clouds. *Proc. Natl. Acad. Sci.* **118**, e2101959118 (2021).
23. B. J. Conrath, Thermal structure of the Martian atmosphere during the dissipation of the dust storm of 1971. *Icarus* **24**, 36–46 (1975).
24. R. M. Ramirez, J. F. Kasting, Could cirrus clouds have warmed early Mars?, *Icarus* **281**, 248–261 (2017).
25. R. M. Ramirez, A warmer and wetter solution for early Mars and the challenges with transient warming. *Icarus* **297**, 71–82 (2017).
26. M. Turbet, C. Gillmann, F. Forget, B. Baudin, A. Palumbo, J. Head, Ö. Karatekin, The environmental effects of very large bolide impacts on early Mars explored with a hierarchy of numerical models, *Icarus* **335**, 113419 (2020).
27. C. M. Dundas, M. T. Mellon, S. J. Conway, I. J. Daubar, K. E. Williams, L. Ojha, J. J. Wray, A. M. Bramson, S. Byrne, A. S. McEwen, L. V. Posiolova, G. Speth, D. Viola, M. E. Landis, G. A. Morgan, A. V. Pathare, Widespread exposures of extensive clean shallow ice in the midlatitudes of Mars. *J. Geophys. Res. Planets* **126**, e2020JE006617 (2021).
28. R. T. Pierrehumbert, *Principles of Planetary Climate* (Cambridge Univ. Press, 2012).
29. A. A. Fedorova, F. Montmessin, A. V. Rodin, O. I. Korablev, A. Määttänen, L. Maltagliati, J.-L. Bertaux, Evidence for a bimodal size distribution for the suspended aerosol particles on Mars. *Icarus* **231**, 239–260 (2014).

30. A. Spiga, F. Forget, S. R. Lewis, D. P. Hinson, Structure and dynamics of the convective boundary layer on Mars as inferred from large-eddy simulations and remote-sensing measurements. *Q. J. Roy. Meteorol. Soc.* **136**, 414–428 (2010).
31. J. R. Murphy, O. B. Toon, R. M. Haberle, J. B. Pollack, Numerical simulations of the decay of Martian global dust storms. *J. Geophys. Res. Solid Earth* **95**, 14629–14648 (1990).
32. D. W. Keith, Photophoretic levitation of engineered aerosols for geoengineering. *Proc. Natl. Acad. Sci. U.S.A.* **107**, 16428–16431 (2010).
33. F. Daerden, J. A. Whiteway, L. Neary, L. Komguem, M. T. Lemmon, N. G. Heavens, B. A. Cantor, E. Hébrard, M. D. Smith, A solar escalator on Mars: Self-lifting of dust layers by radiative heating. *Geophys. Res. Lett.* **42**, 7319–7326 (2015).
34. M. Azadi, G. A. Popov, Z. Lu, A. G. Eskenazi, A. J. W. Bang, M. F. Campbell, H. Hu, I. Bargatin, Controlled levitation of nanostructured thin films for sun-powered near-space flight *Sci. Adv.* **7**, eabe1127 (2021).
35. P. B. Buhler, S. Piqueux, Obliquity-driven CO<sub>2</sub> exchange between Mars' atmosphere, regolith, and polar cap. *J. Geophys. Res. Planets* **126**, e2020JE006759 (2021).
36. R. J. Phillips, B. J. Davis, K. L. Tanaka, S. Byrne, M. T. Mellon, N. E. Putzig, R. M. Haberle, M. A. Kahre, B. A. Campbell, L. M. Carter, I. B. Smith, J. W. Holt, S. E. Smrekar, D. C. Nunes, J. J. Plaut, A. F. Egan, T. N. Titus, R. Seu, Massive CO<sub>2</sub> ice deposits sequestered in the south polar layered deposits of Mars. *Science* **332**, 838–841 (2011).
37. J. C. Stern, B. Sutter, W. A. Jackson, R. Navarro-González, C. P. McKay, D. W. Ming, P. D. Archer, P. R. Mahaffy, The nitrate/(per) chlorate relationship on Mars. *Geophys. Res. Lett.* **44**, 2643–2651 (2017).

38. A. F. Davila, D. Willson, J. D. Coates, C. P. McKay, Perchlorate on Mars: A chemical hazard and a resource for humans. *Intl. J. Astrobiol.* **12**, 321–325 (2013).
39. T. Bertrand, R. J. Wilson, M. A. Kahre, R. Urata, A. Kling, Simulation of the 2018 global dust storm on Mars using the NASA Ames Mars GCM: A multitracer approach. *J. Geophys. Res. Planets* **125**, e2019JE006122 (2020).
40. C. D. O'Connell-Cooper, J. G. Spray, L. M. Thompson, R. Gellert, J. A. Berger, N. I. Boyd, E. D. Desouza, G. M. Perrett, M. Schmidt, S. J. VanBommel, APXS-derived chemistry of the Bagnold dune sands: Comparisons with Gale Crater soils and the global Martian average. *J. Geophys. Res. Planets* **122**, 2623–2643 (2017).
41. O. Forni, M. Gaft, M. J. Toplis, S. M. Clegg, S. Maurice, R. C. Wiens, N. Mangold, O. Gasnault, V. Sautter, S. le Mouélic, P. Y. Meslin, M. Nachon, R. E. McInroy, A. M. Ollila, A. Cousin, J. C. Bridges, N. L. Lanza, M. D. Dyar, First detection of fluorine on Mars: Implications for Gale Crater's geochemistry. *Geophys. Res. Lett.* **42**, 1020–1028 (2015).
42. E. B. Rampe, J. A. Cartwright, F. M. McCubbin, M. M. Osterloo, “The role of halogens during fluid and magmatic processes on Mars” in *The Role of Halogens in Terrestrial and Extraterrestrial Geochemical Processes*, D. Harlov, L. Aranovich, Eds. (Springer Geochemistry, Springer, 2018). [https://doi.org/10.1007/978-3-319-61667-4\\_16](https://doi.org/10.1007/978-3-319-61667-4_16).
43. C. Lang, D. Schüler, D. Faivre. Synthesis of magnetite nanoparticles for bio- and Nanotechnology: Genetic engineering and biomimetics of bacterial magnetosomes, *Macromol. Biosci.* **7**, 144–151 (2007).
44. B. Salmi, 3D—Printing a rocket: I'll never forget the first time I saw a rocket materialize before my eyes, *IEEE Spectrum* **56**, 22–29 (2019).

45. F. H. Koppens, D. E. Chang, F. J. G. de Abajo, Graphene plasmonics: A platform for strong light–matter interactions. *Nano Lett.* **11**, 3370–3377 (2011).

46. B. M. Jakosky, D. Brain, M. Chaffin, S. Curry, J. Deighan, J. Grebowsky, J. Halekas, F. Leblanc, R. Lillis, J. G. Luhmann, L. Andersson, N. Andre, D. Andrews, D. Baird, D. Baker, J. Bell, M. Benna, D. Bhattacharyya, S. Bougher, C. Bowers, P. Chamberlin, J. Y. Chaufray, J. Clarke, G. Collinson, M. Combi, J. Connerney, K. Connour, J. Correira, K. Crabb, F. Crary, T. Cravens, M. Crismani, G. Delory, R. Dewey, G. DiBraccio, C. Dong, Y. Dong, P. Dunn, H. Egan, M. Elrod, S. England, F. Eparvier, R. Ergun, A. Eriksson, T. Esman, J. Espley, S. Evans, K. Fallows, X. Fang, M. Fillingim, C. Flynn, A. Fogle, C. Fowler, J. Fox, M. Fujimoto, P. Garnier, Z. Girazian, H. Groeller, J. Gruesbeck, O. Hamil, K. G. Hanley, T. Hara, Y. Harada, J. Hermann, M. Holmberg, G. Holsclaw, S. Houston, S. Inui, S. Jain, R. Jolitz, A. Kotova, T. Kuroda, D. Larson, Y. Lee, C. Lee, F. Lefevre, C. Lentz, D. Lo, R. Lugo, Y. J. Ma, P. Mahaffy, M. L. Marquette, Y. Matsumoto, M. Mayyasi, C. Mazelle, W. McClintock, J. McFadden, A. Medvedev, M. Mendillo, K. Meziane, Z. Milby, D. Mitchell, R. Modolo, F. Montmessin, A. Nagy, H. Nakagawa, C. Narvaez, K. Olsen, D. Pawlowski, W. Peterson, A. Rahmati, K. Roeten, N. Romanelli, S. Ruhunusiri, C. Russell, S. Sakai, N. Schneider, K. Seki, R. Sharrar, S. Shaver, D. E. Siskind, M. Slipski, Y. Soobiah, M. Steckiewicz, M. H. Stevens, I. Stewart, A. Stiepen, S. Stone, V. Tennishev, N. Terada, K. Terada, E. Thiemann, R. Tolson, G. Toth, J. Trovato, M. Vogt, T. Weber, P. Withers, S. Xu, R. Yelle, E. Yiğit, R. Zurek, Loss of the Martian atmosphere to space: Present-day loss rates determined from MAVEN observations and integrated loss through time. *Icarus* **315**, 146–157 (2018).

47. R. E. Grimm, Low-frequency electromagnetic exploration for groundwater on Mars. *J. Geophys. Res. Planets* **107**, 1-1-1-29 (2002).

48. M. J. Wolff, R. T. Clancy. Constraints on the size of Martian aerosols from Thermal Emission Spectrometer observations. *J. Geophys. Res. Planets* **108**, <https://doi.org/10.1029/2003JE002057> (2003).
49. H. Iwabuchi, P. Yang. Temperature dependence of ice optical constants: Implications for simulating the single-scattering properties of cold ice clouds. *J. Quant. Spectrosc. RA* **112**, 2520–2525 (2011).
50. M. R. Querry, Optical constants. US Army Armament, Munitions & Chemical Command, Chemical Research & Development Center (1985).
51. A. D. Rakić, Algorithm for the determination of intrinsic optical constants of metal films: Application to aluminum. *Appl. Optics* **34**, 4755–4767 (1995).
52. J. Cahill, D. T. Blewett, N. V. Nguyen, A. Boosalis, S. J. Lawrence, B. W. Denevi, Optical constants of iron and nickel metal and an assessment of their relative influences on silicate mixture spectra from the FUV to the NIR. *Icarus* **317**, 229–241 (2019).
53. F. Neubrech, A. Pucci, Plasmonic enhancement of vibrational excitations in the infrared. *IEEE J. Select. Topics Quant. Electron.* **19**, 4600809 (2013).
54. L. Novotny, Effective wavelength scaling for optical antennas. *Phys. Rev. Lett.* **98**, 266802 (2007).
55. J. Kasting, D. Whitmire, R. Reynolds, Habitable zones around main sequence stars, *Icarus* **101**, 108–128 (1993).
56. S. Manabe, R. T. Wetherald, Thermal equilibrium of the atmosphere with a given distribution of relative humidity. *J. Atmosph. Sci.* **24**, 241–259 (1967).
57. M. P. Thekaekara, Solar energy outside the Earth's atmosphere. *Solar Energy* **14**, 109–127 (1973).

58. R. M. Ramirez, R. Kopparapu, M. E. Zugger, T. D. Robinson, R. Freedman, J. F. Kasting, Warming early Mars with CO<sub>2</sub> and H<sub>2</sub>. *Nat. Geosci.*, **7**, 59–63 (2014).
59. M. A. Mischna, C. Lee, M. Richardson, Development of a fast, accurate radiative transfer model for the Martian atmosphere, past and present. *J. Geophys. Res. Planets*, **117**, <https://doi.org/10.1029/2012JE004110> (2012).
60. E. Millour, F. Forget, F. González-Galindo, A. Spiga, S. Lebonnois, S. R. Lewis, L. Montabone, The Mars climate database (version 4.3). No. 2009-01-2395. SAE Technical Paper, 2009.
61. S. D. Guzewich, E. R. Talaat, A. D. Toigo, D. W. Waugh, T. H. McConnochie High-altitude dust layers on Mars: Observations with the Thermal Emission Spectrometer. *J. Geophys. Res. Planets*, **118**, 1177–1194 (2013).
62. S. D. Guzewich, A. D. Toigo, M. I. Richardson, C. E. Newman, E. R. Talaat, D. W. Waugh, T. H. McConnochie The impact of a realistic vertical dust distribution on the simulation of the Martian General Circulation. *J. Geophys. Res. Planets*, **118**, 980–993 (2013).
63. S. D. Guzewich, C. E. Newman, M. D. Smith, J. E. Moores, C. L. Smith, C. Moore, M. I. Richardson, D. Kass, A. Kleinbohl, M. Mischna, F. J. Martin- Torres, M.-P. Zorzano-Mier, M. Battalio, The vertical dust profile over Gale Crater, Mars. *J. Geophys. Res. Planets* **122**, 2779–2792 (2017).
64. S.-Y. Hong, H.-L. Pan, Nonlocal boundary layer vertical diffusion in a medium-range forecast model. *Mon. Wea. Rev.* **124**, 2322–2339 (1996).